Noname manuscript No.
(will be inserted by the editor)

On crack nucleation and propagation in elastomers: I. *In situ* optical and x-ray experimental observations

Jinlong Guo · Krishnaswamy Ravi-Chandar

Received: date / Accepted: date

Abstract This article presents the results of an investigation of crack nucleation and propagation in a transparent polydimenthylsiloxane (PDMS) elastomer. The main objective of the investigation is to characterize quantitatively the evolution of crack nucleation and propagation behavior not just through the usual macroscopic load and displacement data, but with synchronized optical images at high spatial and adequate temporal resolution that will resolve the evolution of the failure processes. This is augmented with x-ray computed tomography (CT) scans to characterize the three-dimensional geometry of the cracks nucleated in the interior of the elastomer.

Towards this goal, we reproduce the classical *poker-chip* experiment of Gent and Lindley (1959) in which the specimen's diameter-to-thickness ratio is varied over a broad range to cover crack nucleation, propagation, and their coalescence. These experiments are performed on transparent PDMS with different compositions, first in a specially built loading machine that is fitted with a high magnification microscopic camera that permits the measurement of the load while simultaneously providing images of the specimen configuration and subsequently in an apparatus built for *in situ* observations using an x-ray CT scanning system.

These experiments reveal that nucleation of multiple microcracks dominates when the diameter-to-thickness aspect ratio α is sufficiently large, because the incompressibility of the material induces substantial, nearly uniform hydrostatic tension in the specimen. In contrast, specimens with smaller aspect ratio tend to nucleate fewer cracks, and are dominated by the growth of these cracks. At even smaller α, the hydrostatic stress is significantly lowered and failure is dominated by surface flaws. The three-dimensional geometry, and the spatial distribution of the nucleated cracks were evaluated using optical microscopy and x-ray CT scans. This revealed cracks of three different shapes, one of which was confined in a layer near to the upper or bottom boundary of the poker-chip, another was across the thickness, but with a tilt relative to the axis of the specimen, and the last was propagating along the radial direction.

Keywords cavitation · fracture · polydimethylsiloxane

J. Guo · K. Ravi-Chandar (✉)
Department of Aerospace Engineering and Engineering Mechanics, Center for Mechanics of Solids, Structures, and Materials, University of Texas at Austin, Austin, TX 78712-1221, USA
E-mail: ravi@utexas.edu

1 Introduction

Elastomers constitute a class of materials of considerable interest, due not only to their numerous applications in our daily life, but also their ubiquitous role in the fundamental study of the reversible/irreversible mechanical behaviors. In this work, we aim to provide a new perspective on elastomers (more specifically cross-linked silicone elastomer, polydimethylsiloxane (PDMS)) under the triaxial loading state, from the pristine state towards the fracture initiation and growth and eventual failure, by leveraging a confined geometry under uniaxial stretch, or the so-called *poker-chip* experiment.

This problem has a long history in that it has been studied since Busse (1938) and Yerzley (1939), who examined synthetic rubber in a sandwich structure of two rigid steel clamps for the corresponding adhesive property; it later inspired Gent and Lindley (1959) to investigate the internal rupture of natural rubber on the poker-chip specimen that induces a large triaxial

stress state inside of the domain. The authors noticed a strain softening in the load-deflection curve during the loading, and they conjectured that it is the initial internal flaw that undergoes a rapid *elastic* expansion inside of the rubber due to the large hydrostatic stress; this became well known later as the cavitation instability in elastomers. To understand the cavitation criterion, they further simplified the original boundary value problem to a local representative problem – the unbounded growth of a finite-size spherical cavity in an infinite shell under a far-field negative pressure (hydrostatic tension) inspired by the solution from Green and Zerna (1992); the theory seemed to be corroborated qualitatively by part of the experiment results. With a Neo-Hookean material model, the hydrostatic criterion of cavitation instability is $P_{cr} = 5\mu/2$, where μ is the initial shear modulus. Ever since the pioneering work of Gent and Lindley (1959), extensive studies have emerged to interpret and predict the cavitation from the viewpoint of elasticity; especially in Ball (1982), the equivalent problem of solving the bifurcated discontinuous solution of a unit solid sphere under radially symmetric load has been addressed. Moreover, the general setting of non-axisymmetric geometry and loading state has also been explored by Horgan and Abeyaratne (1986), Sivaloganathan (1986), James and Spector (1991) and Lopez-Pamies et al. (2011).

However, from the experiments of Gent and Lindley (1959), and as recognized by Gent (1990) himself, the conclusion that a hydrostatic stress exceeding the cavitation threshold will always nucleate an interior cavity/crack does not appear to be correct. An obvious drawback of the purely elasticity-based criterion is the fact that the local stretch of the cavitation nuclei is of the order of 100, but the polymer chains cannot be stretched to such extent without disentanglement or bond breaking, making it essential to account for fracture or bond rupture and to include the fracture energy into the problem.

The first study of this type goes back to Williams and Schapery (1965). They introduced a length scale (the initial cavity radius, A) into the nucleation criterion via the fracture energy, Γ, per unit undeformed area. While this criterion brings size dependence, it converges to the hydrostatic criterion when $\frac{2\Gamma}{\mu A}$ is sufficiently large, and is unable to explain the observed cavitation condition. Gent and Tompkins (1969b) and Gent and Wang (1991) have addressed this problem through incorporation of both surface tension and Griffith's energy balance approach to fracture. Even though these considerations bring size dependence to the cavitation criterion and explains why the initial cavity with smaller size is more inclined to inflate first, they fail to clarify why the local negative pressure from the experiment greatly surpasses the prediction of $5\mu/2$, see Gent and Tompkins (1969a) without nucleating cavities.

Numerous articles in the literature address different aspects of the cavitation problem, both theoretical/numerical (Ball (1982), Sivaloganathan (1986), Müller and Spector (1995), Lin and Hui (2004), Lefèvre et al. (2015), and Kumar and Lopez-Pamies (2021)). Despite these efforts, a predictive criterion for the onset of interior cavity or crack nucleation that spans the entire range of sizes of defects is still not available. To date, Kumar and Lopez-Pamies (2021) appear to have developed the first theoretical/numerical work that could reproduce the experimental observation of the distribution of interior fracture nucleation and subsequent growth, with the macroscopic mechanical response. Their work posits that nucleation of fracture in poker-chip experiments is governed by the strength of the elastomer, while the propagation of fracture is governed by the Griffith competition between the bulk elastic energy of the elastomer and its surface fracture energy.

While there exists a large literature from different theoretical and numerical points of view, very few studies on the poker-chip experiment have been conducted, except for Lindsey et al. (1963) and Lindsey (1966); these authors used a transparent polyurathane to observe cavitation and further crack growth, and provided limited insight on the nucleation and growth. A *poker-chip like* geometry has been implemented recently, for example in Lakrout et al. (1999), Shull and Creton (2004), and Bayraktar et al. (2008), but a systematic and fundamental study, focused on the interior bulk nucleation for the isotropic hyper-elastic incompressible material with varying geometric constraints, is needed and is the main objective of this work.

In this investigation, we recreate the classical poker-chip experiment with the transparent PDMS elastomer and exploit synchronized mechano-optical and x-ray computed tomography observations to trace the fracture initiation and further propagation. In Sect. 2, the experimental set-up and protocol are introduced, including two apparatus designs, sample preparation, experimental protocol and data processing. Next in Sect. 3, the *in situ* direct optical observations are focused on the nucleation and growth of cavities/cracks; results from four representative samples that span the entire transition of the onset of fracture, from surface nucleation to interior nucleation with different growth regimes. In Sect. 4, a detailed description of the location and geometry of the crack nucleation and growth inside of the sample is provided based on the x-ray image analysis. This is followed in Sect. 5 by a description of the entire process of nucleation, growth and coalescence of

cracks in poker-chip specimens of different diameter-to-thickness ratios. The quantitative analysis and characterization of crack nucleation based on the observations of two-dimensional projection from the microscope, and of three-dimensional geometric features of the cracks are provided in Sect. 6. Finally, the experimental observations and theoretical interpretations are summarized in Sec. 7.

A detailed derivation and calculation of the fracture nucleation criterion and a full-field numerical simulations based on the variational phase field model in comparison with the collected experimental observation will be presented in the companion article.

2 Experimental set-up and protocol

2.1 Specimen design

The poker-chip specimen design of Busse (1938), Yerzley (1939), and Gent and Lindley (1959), is a variant of the ASTM-D-429 standard from 1935; it consists of two cylindrical metal grips attached to a cylindrical rubber specimen with a thickness T and diameter D. The aspect ratio is defined as $\alpha := D/T$. This arrangement does not permit observation of the progression of nucleation and growth of damage in the interior, but only global load-elongation measurement as well as the final failure surface. In this work, the metal grips were replaced with polymer grips to facilitate such observations[1]; the design is shown in Fig. 1. The top grip is made of a translucent polycarbonate (PC) cylinder to provide a diffuse optical background while the bottom grip is made of an optically transparent polymethylmethacrylate (PMMA) to provide a clear viewing path from below. The top grip is attached to the loading machine through the threaded connection while the bottom grip is connected to the loading machine through a set of four pins inserted into mating holes in the PMMA cylinder. The PC and PMMA materials may be assumed to be rigid relative to the PDMS[2].

2.2 Specimen preparation

The PDMS base (Dow Corning Sylgard 187) and curing agent were mixed in a nominal 30:1 ratio (by weight) in a paper cup, stirred for 15 minutes and then degassed for about 45 minutes to extract trapped air from the mixture. These timings correspond to a 10 g mix of the polymer; they would have to be adjusted based on the amount of polymer to be mixed. The surfaces of the two grips that are to be adhered to the specimen were cleaned with ethanol to remove contaminants. These surfaces were then coated with a thin layer of Dow Corning 92-023 primer and allowed to dry at room temperature for more than 30 minutes. This primer coating is essential in the preparation of the poker-chip specimen since it prevents delamination or interfacial fracture and allows for damage to nucleate in the interior of the specimen. In order to make a specimen mold, a thin transparent polymer sheet was used to wrap around the PMMA grip to form a cylindrical mold. The PDMS liquid was then poured into this mold without generating air bubbles; then the PC grip was slipped on top and allowed to settle on the liquid PDMS layer, carefully avoiding trapping of air between the two; note that the thickness of the PDMS layer is manually controlled simply by controlling the volume of PDMS poured into the mold. Finally, the samples are cured at 80 °C for 12 hours, and then allowed to relax at room temperature for an additional 12 hours prior to testing.

The manufacturing process described above results in the formation of a clear PDMS layer, strongly bonded between the two end grips. Optical clarity implies that air bubbles, if present, are likely to be below a few 100 nm in size. However, there are two other types of defects that were observed in the specimens. First, isolated, large air bubbles (≈1 mm in diameter) developed near the outer cylindrical boundary of the poker-chip specimen during the curing process in some specimens; however, these had very little influence on the nucleation of damage in the interior of the specimen, as we will show later through direct observation[3]. Second, some variability in the thickness of the PDMS layer was observed, especially in the specimens with a larger aspect ratio; as a result, all specimens may not be perfectly axisymmetric; however, from the x-ray measurements, we can determine that these imperfections are small enough to be negligible.

2.3 Apparatus and experimental protocol

Two different apparatuses were built to perform the poker-chip experiments. Apparatus A was designed to collect high magnification optical images synchronously with the measurement of the macroscopic mechanical

[1] Lindsey et al. (1963) have used a similar approach and observed the nucleation of cracks

[2] The Young's moduli of PC and PMMA are 2.4 GPa and 2.9 GPa, respectively, while the PDMS elastomer has an initial modulus on the order of 0.1 MPa

[3] Lindsey (1966) introduced bubbles and demonstrated that their influence on the response was indeed negligible. Also, it is difficult to achieve higher spatial and temporal resolution; given this limitation, the identified event is an upper bound for the nucleation of the crack.

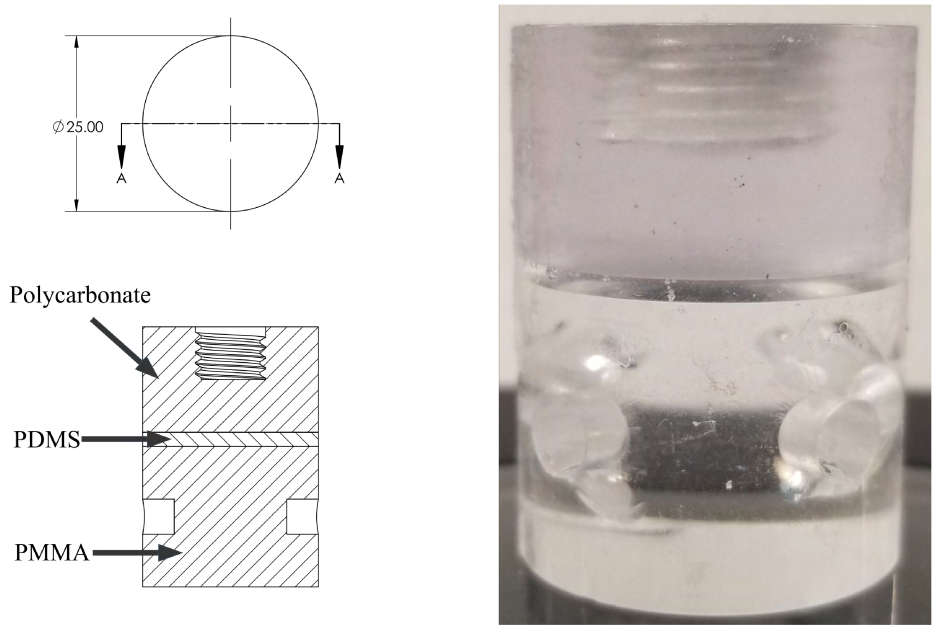

Fig. 1: The drawing on the left column shows the poker-chip specimen (labeled PDMS), a 25mm-diameter cylinder. The top grip is made of polycarbonate and has a threaded side for connection to the loading machine; the bottom grip is made of a transparent PMMA and is fitted with four symmetric slots for attaching to the bottom of the loading frame. A picture of a manufactured specimen is shown on the right column.

response by integrating a Keyance microscope with an Instron test machine. Apparatus B was designed to shed light and quantify the geometry of the interior nucleation and growth of damage in three-dimensions by integrating a mechanical loading frame into an x-ray CT scanner. The corresponding designs and experimental protocol are described below.

2.3.1 Apparatus A

The Apparatus A was built around an Instron test machine to control the loading rate and obtain precise load-deflection data by using the load-cell data coupled with Digital Image Correlation (DIC) for measuring the specimen displacement. In order to observe and record the nucleation and growth of damage at high spatial resolution, the whole loading apparatus was built into the Instron machine with a Keyence Model VHX 5000 microscope mounted from below as shown in Fig. 2, providing a two dimensional projected view of the poker-chip specimen through the bottom PMMA grip. Full view of the specimen viewed through the Keyance microscope is shown in the lower right image in Fig. 2. The diameter of the specimen is outlined by a white dashed circle; the view is interrupted slightly by the four loading pins inserted into the lower PMMA grip as identified in the figure. The background illumination is brighter in the regions where the upper PC grip has a screw thread machined into it.

There are two major sources of inaccuracy that need to be overcome during the poker-chip experiment - undesirable transverse loading resulting from misalignment and machine compliance, see Lindsey et al. (1963) and Lakrout et al. (1999). To resolve the first issue, we set an additional degree of freedom by slightly loosening the aluminum ring that is used to fix the poker-chip sample with the ground plate, and providing a universal joint while attaching the top grip to the Instron load cell. To take account of the machine compliance, printed speckles were attached on the PC and PMMA grips, and DIC was used to determine the actual displacement across the poker-chip specimen.

Experimental protocol Before each test, the initial thickness of the specimen was measured and the sample was assembled into the apparatus; a reference image was captured in the microscope. Subsequently, the load was increased manually until the specimen seated at the grips and a small pre-load was measured. Thereafter the top grip was moved with a cross-head speed of 0.2 mm/min (this corresponds to a stretch rate less than 0.016/s which can be considered as quasi-static). Simultaneously, the side camera started to capture images of the speckles on the top and bottom grips once every 5 seconds for determining the displacement across the

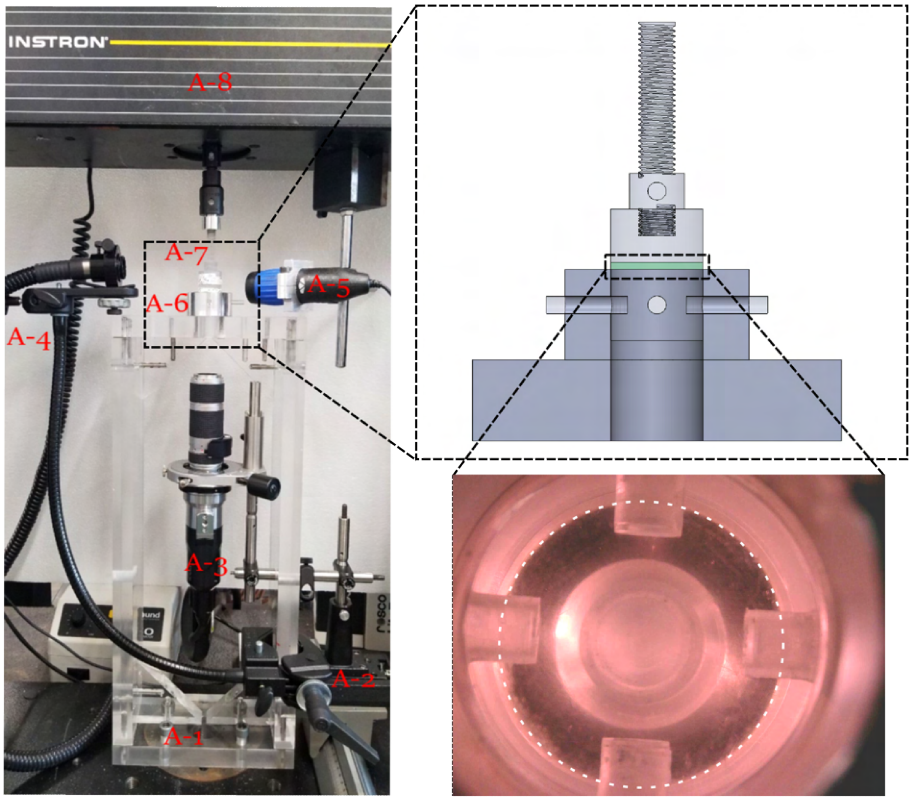

Fig. 2: Apparatus A: A-1: Frame made of PMMA plates for attaching the poker chip specimen fixture to the Instron floor; A-2: Adjustable support for mounting the Keyence microscope (A-3); A-4: high intensity lighting; A-5: video microscope for imaging grip displacement; A-6: Poker chip test fixture (shown as a drawing in the top right); A-7: connection to the Instron load cell (5 kN capacity); A-8: Instron cross-head. Lower right image is an example of the image obtained with the Keyence microscope; the dotted line indicates the diameter of the specimen.

specimen. Subsequently, the Keyance microscope images were captured at 15 frames per second, starting at a threshold value of the load (typically 20 to 30 N). All data were synchronized for data processing. During the stretch, crack nucleation could be identified from the image contrast and sometimes also by the slope change of the load-deflection curve. After passing the first nucleation, the stretching of the specimen continued with the same rate, and the further growth of the nucleated crack, and subsequent nucleation, if any, will be detected also from the contrast change of the microscope image and the load data evolution.

2.3.2 Apparatus B

One of the best tools to detect interior damage and reconstruct its 3D geometry in a nondestructive manner is through the micro x-ray computed-tomography (CT), which relies on differences in the mass densities (and hence attenuation) among different objects, e.g. voids and elastomer matrix in the present case. Tomographic images "cutting" along certain directions are produced and used for the reconstruction of the complete 3D geometry. For further details, interested readers are directed to Buffiere et al. (2010) who provide a comprehensive review on the micro CT technique. There is a rich literature studying interior nucleation and propagation via x-ray scan for both brittle and ductile materials, (see, for example, Toda et al. (2011) and Liu and Sancaktar (2018)). Also cavitation in rubble-like materials has been examined (see Bayraktar et al. (2008) and more recently by Euchler et al. (2020)). However, these are focused on the fracture morphology and microscopic geometry with limited investigations on the nucleation criterion and further growth.

Apparatus B is a manually operated mechanical loading device, (see details in Fig. 3) that allows the *in situ* x-ray scanning. In other words, the deformed configuration of the entire interior domain of the poker chip specimen is captured well with the resolution of 10 μm.

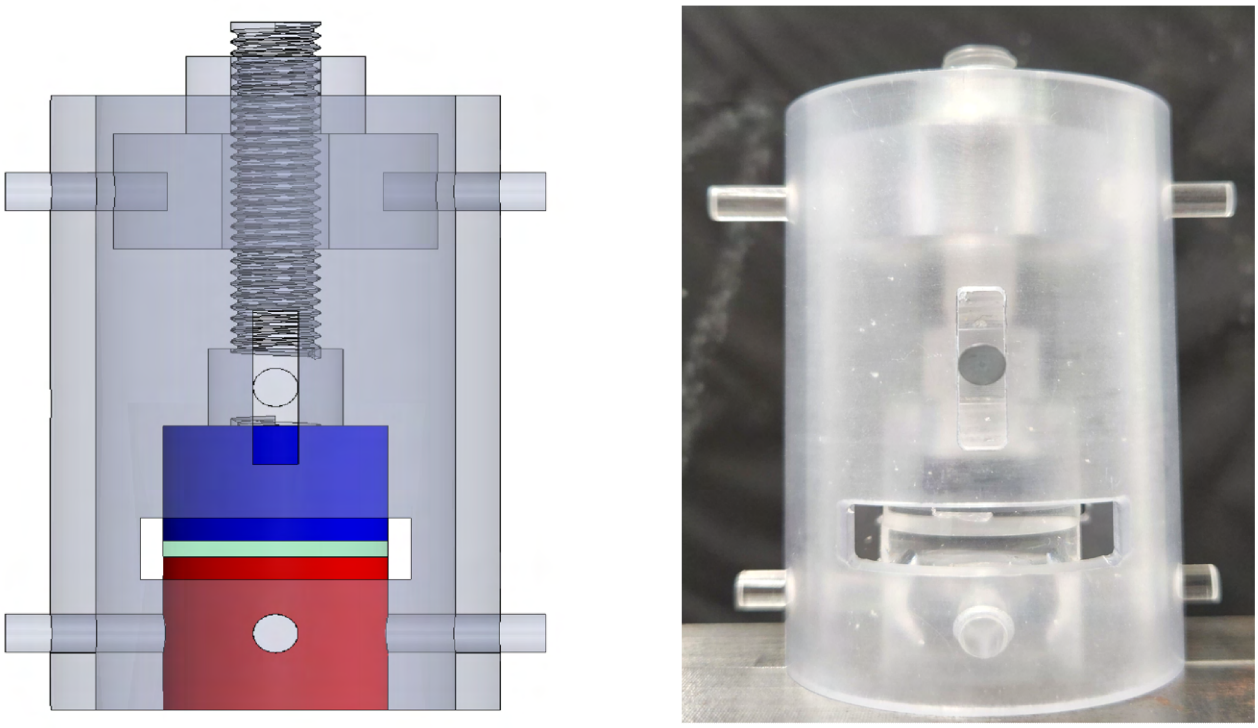

Fig. 3: Apparatus B: an outer hollow cylinder made of polycarbonate is utilized as a rigid reference. Four short pins were used to fix the PMMA grip (red) to the outer cylinder, and the polycarbonate grip (blue) is connected by a screw-cut cylinder, which is fixed by a slot on the hollow cylinder with a through shaft. On the other end of the hollow cylinder, a screw helps to apply a displacement boundary condition to the sample (light blue-green), since the bolt cannot move forward due to the front shield.

Experimental protocol As discussed for Apparatus A, the initial configuration of each sample (thickness and cross-section) was captured with Keyence microscope. Next we carefully twisted the loading bolt in small increments to apply the uniaxial stretch.

With each increment of loading, the deformed specimen was viewed with the microscope to identify nucleation of damage. When the first cavity was observed, the specimen was promptly unloaded by a small amount, in order to prevent the subsequent growth of damage. However, the undeformed configuration of the crack or damage cannot be captured, since the interior microcracks can close and become invisible to the x-ray scanning (see Poulain et al. (2018) who demonstrated that cracks in PDMS close upon unloading and even heal completely). Once the crack was formed, the specimen, still mounted in the loading apparatus, was placed in the x-ray chamber to obtain the CT images.

It is necessary to perform image analysis to obtain quantitative measurements of the size and distance of each bubble-like features from the microscopic images; these are effectively processed with image processing and other tools in MATLAB. In addition, we reconstruct the 3D geometry of the interior cracks from x-ray CT images as shown in Sec. 4; the reconstruction is generally realized with an ellipsoid fit after essential pre-processing, such as smoothing and binarizing. The whole procedure is largely based on software packages ImageJ (Schindelin et al. (2012)) and 3DSlicer (Kikinis et al. (2014)).[4]

3 Nucleation and growth of cracks under *triaxial* loading: Optical observations

We now turn to reporting the observations of initiation and growth of damage/fracture during the poker-chip experiment performed with Apparatus A and the corresponding experimental protocol. About one hundred and twenty experiments were performed on specimens with different aspect ratios within the range of

[4] The original tomographic image stack in tiff-format was denoised with Gaussian filter of radius in [10,20] pixels in ImageJ, which was followed by a binarization with the default threshold method; the thresholded images were thereafter imported to 3D Slicer for segmentation and quantitative measurement of each crack of interest via segmentation-related modules and python scripts.

$\alpha \in (2, 75)$, and different PDMS compositions including 20:1, 30:1, and 45:1. The observed response, in terms of the nucleation and growth of damage/fracture, falls into four categories: (i) surface crack nucleation and growth, (ii) single interior crack nucleation and growth, (iii) multiple interior crack nucleation and growth, and (iv) numerous interior crack nucleation. In this section, observations from tests performed on four samples of 30:1 resin-to-curing agent ratio with progressively increasing aspect ratio are described. Specimens with other compositions exhibited qualitatively similar behavior. In each case, we present the load-versus-time curve, where the load is divided by the initial cross-sectional area, indicated as S. Also, sequences of images that are selected from the recording of the Keyence microscope (temporal and spacial resolutions are 15 frames/second and 16 μm/pixel respectively) are presented. The full video recordings are available in the Supplementary Material.

	Test	Aspect ratio	Composition ratio
Optical	A	4.7	28.5
	B	8.9	30.0
	C	11.3	29.5
	D	41.6	29.5
X-ray	E	8.2	28.4
	F	18.4	31.2
	G	75.7	28.4
	H	10.2	20.0

Table 1: Summary of 8 tests described in Sec. 3 and Sec. 4 including the aspect ratio and composition ratio. Note that the composition of Test H is 20:1, but exhibits a similar qualitative response as the specimens with a 30:1 composition.

3.1 Test A: Surface crack nucleation

A specimen of 5.3 mm thickness with $\alpha = 4.7$ was examined based on the preceding protocol; we will label this as Test A. Fig. 4a shows the normalized load as a function of time with an expanded view of the curve near the maximum load point. Fig. 4b shows selected microscopic images corresponding to the times labeled in Fig. 4a. In the beginning of the test, at Frame 15, no *interior* defects were detected except for an initial cavity sitting near to the free boundary of the specimen as indicated in the figure; it has a negligible effect on the overall response of the specimen as will become evident later. Configuration b corresponds to a normalized force of $S = 0.127$ MPa. A small defect emerges near the top, identified in the black box in Frame 7245; a magnified view of this region is shown in the left column, highlighting the feature by a red circle. Notice that it is *not* an interior nucleation but surface nucleation of a crack. About 40 seconds later (Frame 7800, configuration c), the crack has grown to an elliptical shape, while the corresponding load has reached a global maximum $S_{max} = 0.13$ MPa. In another 10 seconds (Frame 7965, configuration d), the crack grew to a size of 5 mm; meanwhile a second surface crack nucleated near the bottom of the image. In configurations e and f, the two cracks spread towards the central region in a stable manner and merge, creating rough fracture surfaces. Through all of this loading, the initial cavity remains unaltered, indicating that this defect did not alter the response of the specimen significantly. This kind of response - nucleation and growth of one or more surface cracks - was observed in repeated experiments when the aspect ratio α was in the range of 2 to 7.

3.2 Test B: Single interior crack nucleation, dominated by crack growth

We describe next, the response of a sample with thickness $t = 2.8$ mm, and aspect ratio $\alpha = 8.9$, with the same experimental protocol as before; we will label this as Test B. The normalized load as a function of time and selected microscopic images are shown in Fig. 5. The specimen did not have any *macroscopically* visible defects initially as can be seen from the image at Frame 15 (configuration a). With loading, the first optically detectable defect was nucleated in Frame 2270 (configuration b) as identified in the black square, and shown at a greater magnification for easy visualization; the size of this feature is already of about 100 μm in the major axis[5]. With continued increase of the crosshead displacement, through Frames 2360 (configuration c) and 2430 (configuration d), the defect emerges into a clearly identifiable elliptical shape[6] and increasing in size to nearly 1 mm, while the macroscopic load continues to increase; clearly, the nucleation of the interior crack alone was inadequate in softening the global response; however, when the crack grows to a size comparable to the specimen thickness, the load begins to drop.

Continued loading beyond Frame 2430 leads to a maximum load of $S_{max} = 0.151$ MPa at Frame 2450

[5] We refrain from calling these cavities because by the time the intrinsic defects of size 10 to 100 nm grow to a visible size of 10 to 100 μm, it must have transitioned into a crack

[6] We know from x-ray CT scans described later that these are actually ellipsoidal

Fig. 4: Test A, surface crack nucleation

(a) Normalized force versus time for Test A with $\alpha = 4.7$. The blue solid line represents the entire curve, and 6 deformed configurations (a to f) are marked with red circles. The region near the peak load is magnified in the inset.

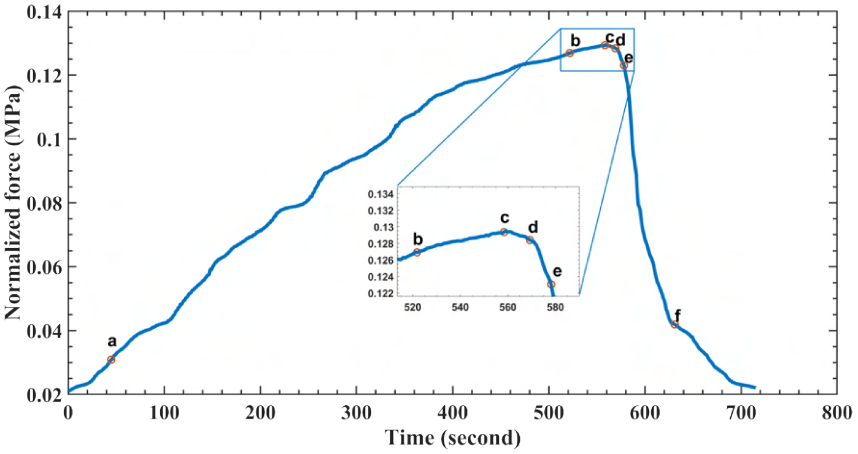

(b) Selected sequences of images from Configuration a to f in Test A illustrating the surface nucleation, where the first nucleation is marked by a red circle in the magnified figure beside the image sequence.

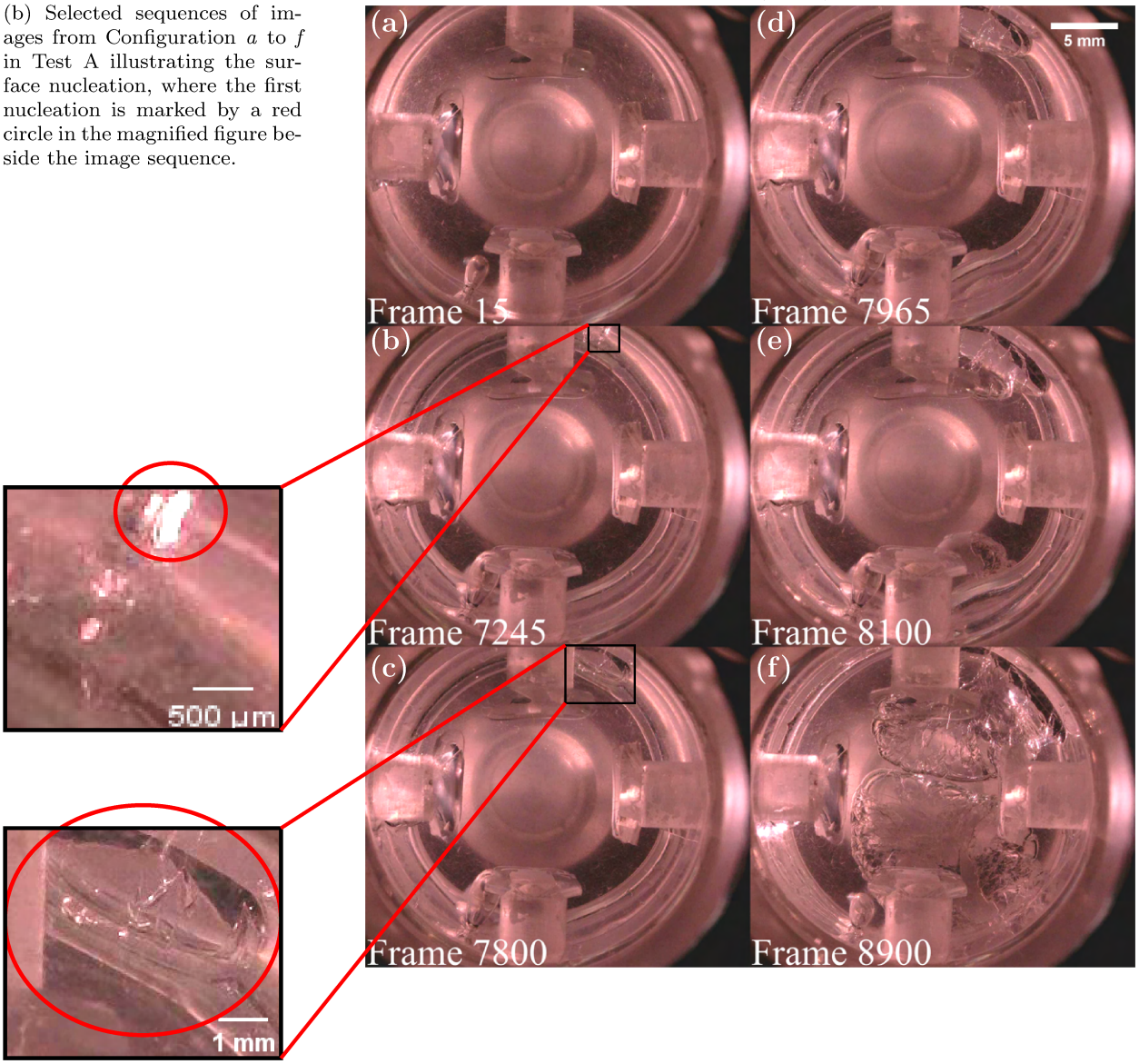

Fig. 5: Test B, single interior nucleation

(a) Normalized force versus time for Test B with $\alpha = 8.9$, with data of 8 configurations marked with red circle symbols.

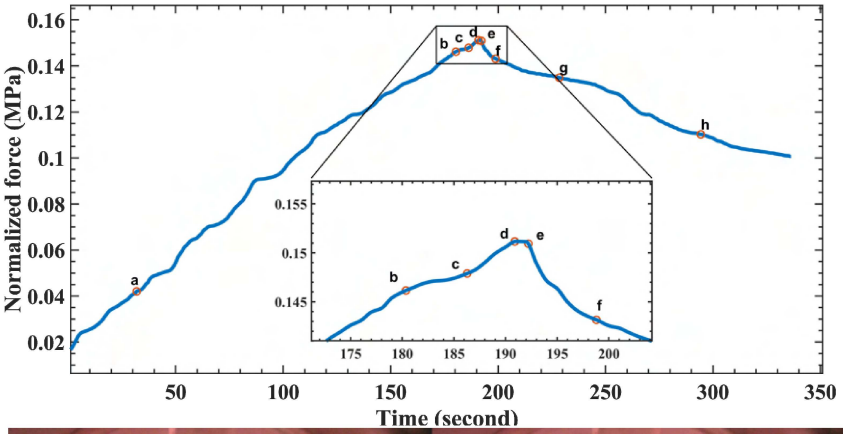

(b) Selected sequences of images in Test B illustrating the interior crack nucleation and further growth.

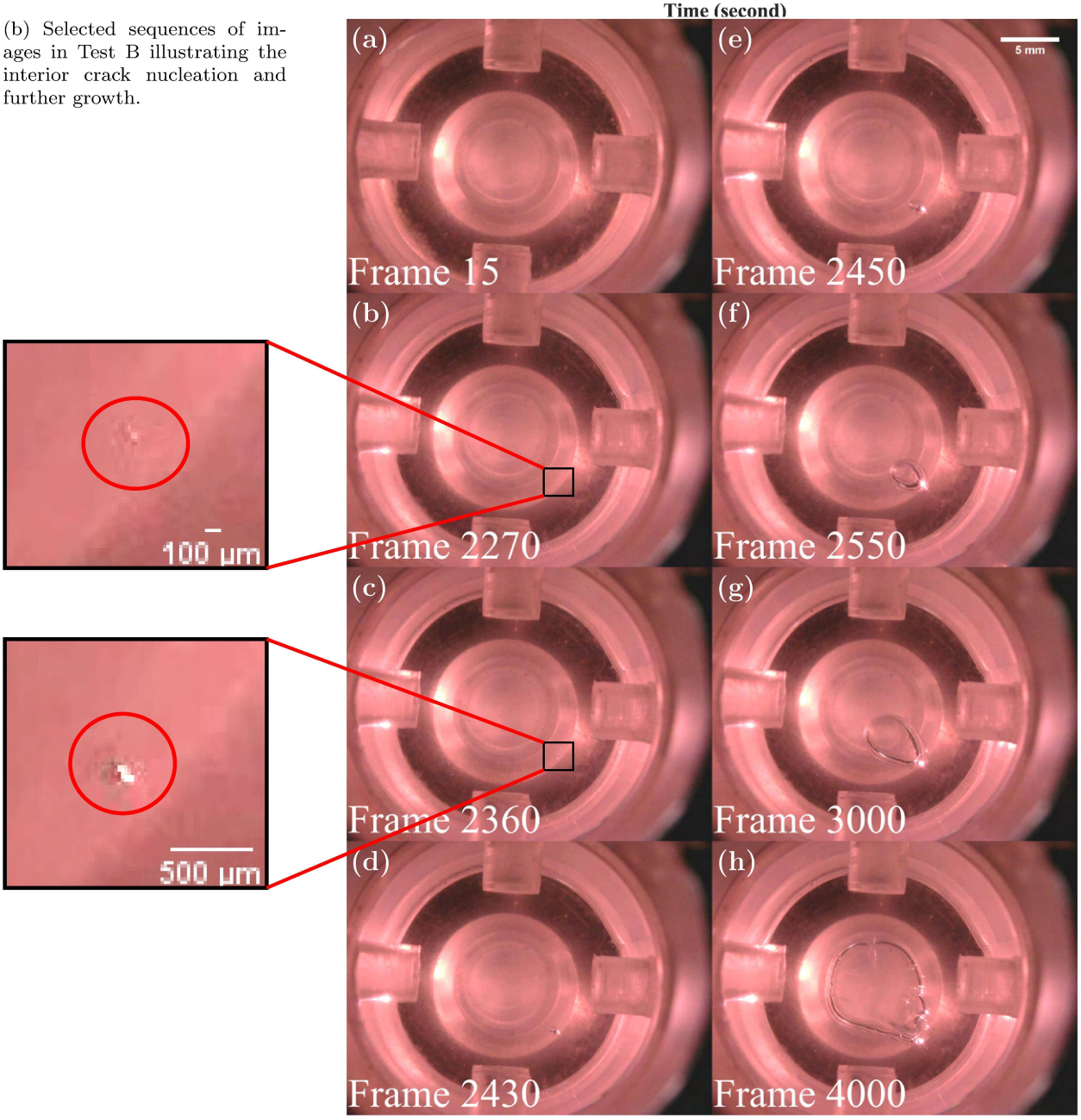

Fig. 6: Test C, multiple interior crack nucleation

(a) Normalized force versus time for Test C with $\alpha = 11.3$, where the selected configurations are marked with red circle, green triangle, and yellow diamond for different phases with varied numbers of existing cracks.

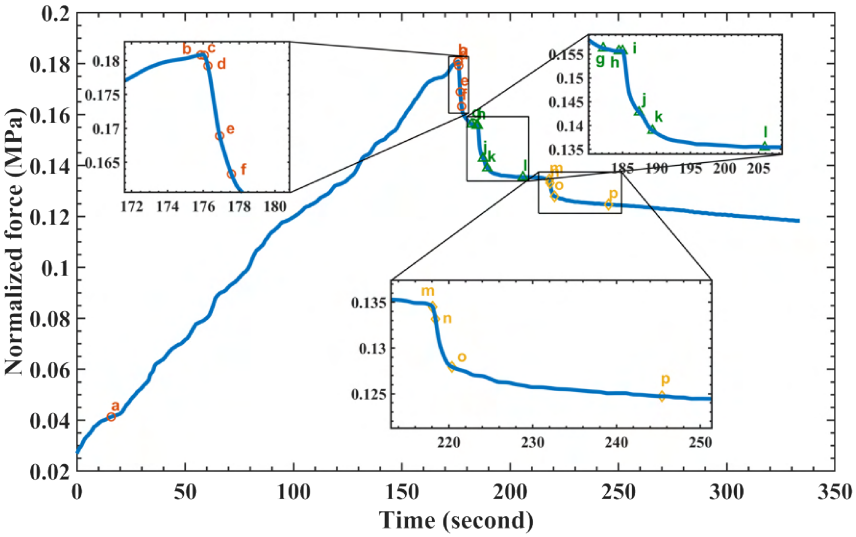

(b) Selected sequences of images in Test C illustrating the first interior crack nucleation and growth.

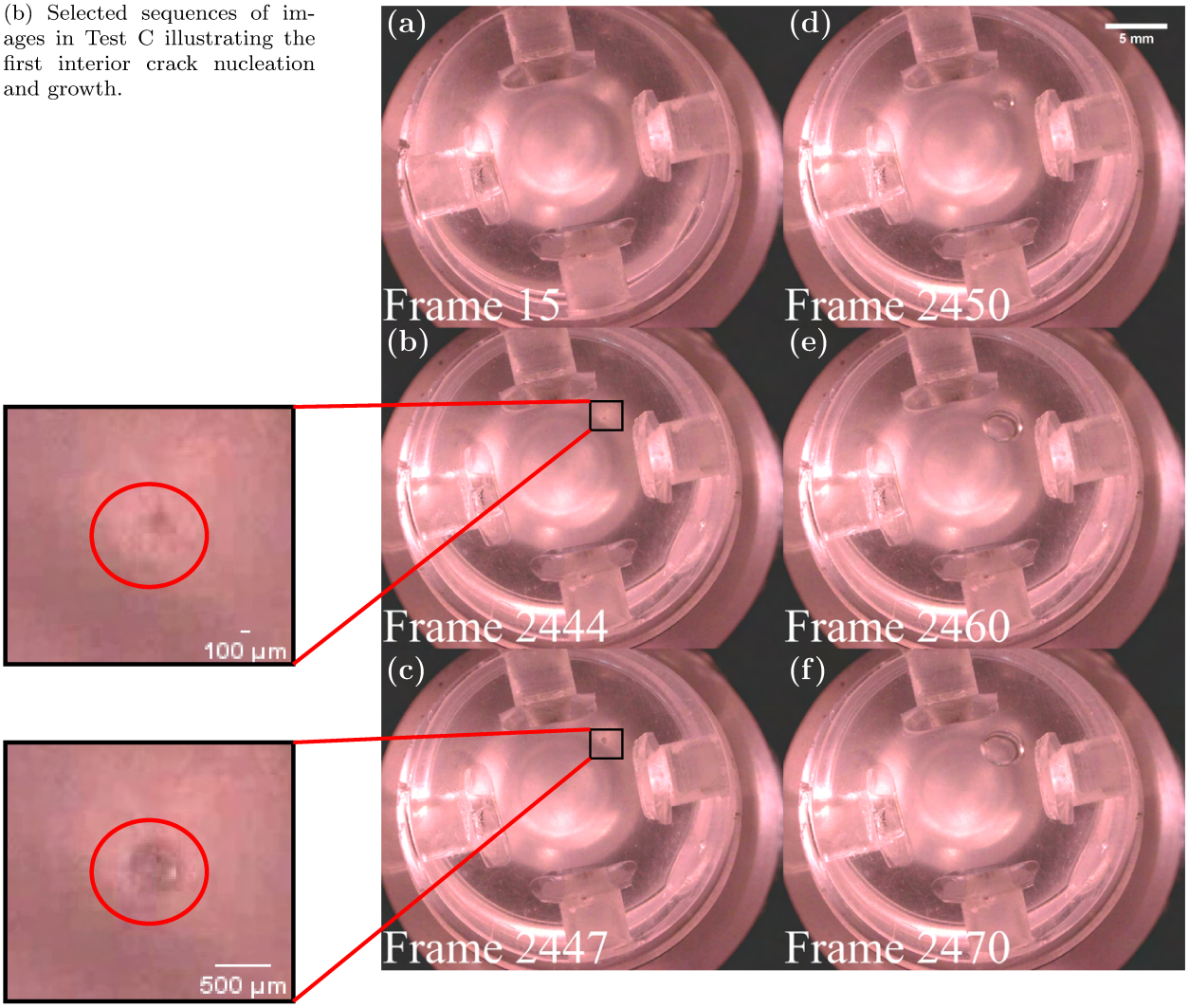

(c) Selected sequences of images in Test C illustrating the second interior crack nucleation, and two-crack influence.

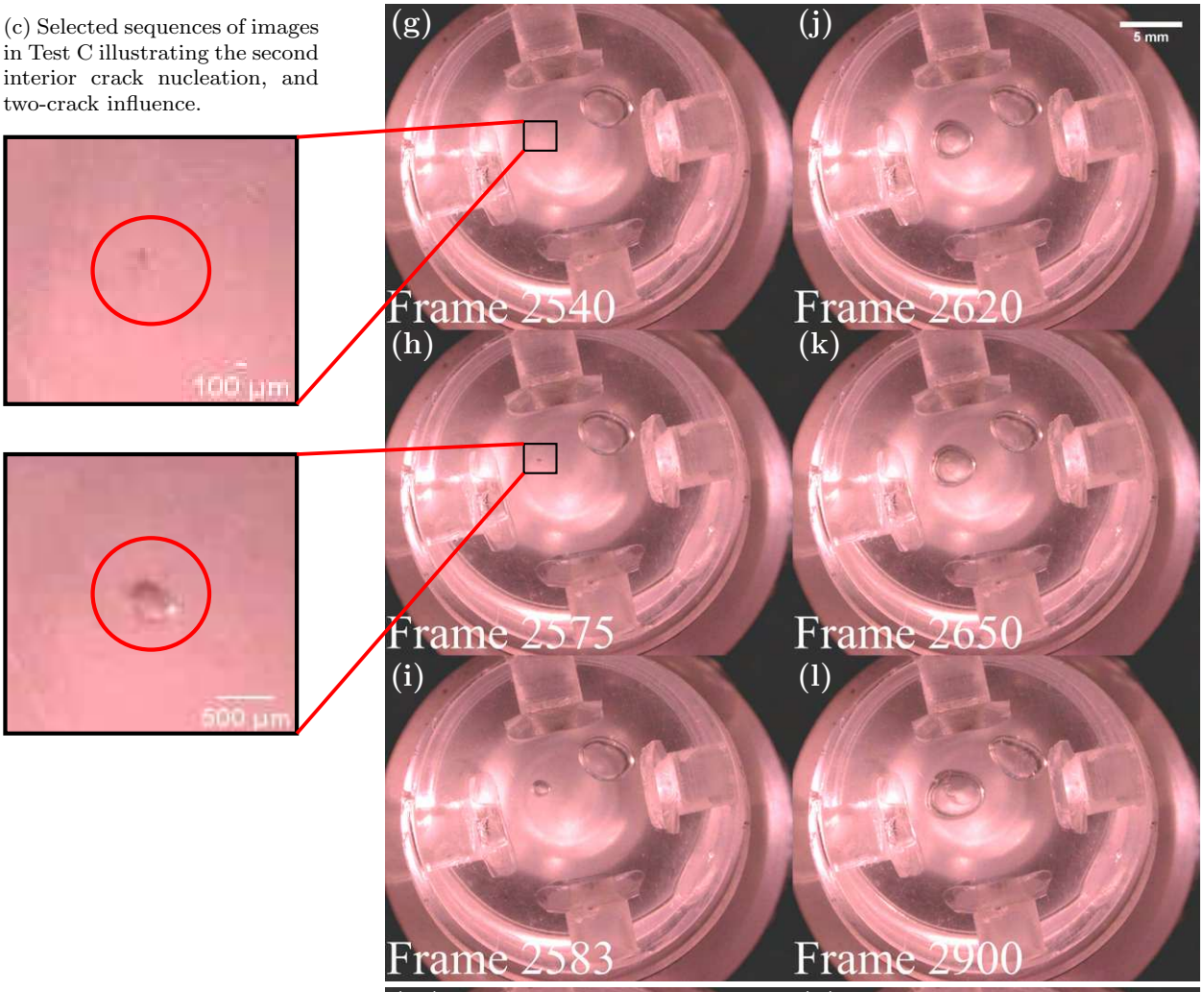

(d) Selected sequences of images in Test C illustrating the third interior crack nucleation, and three-crack interaction.

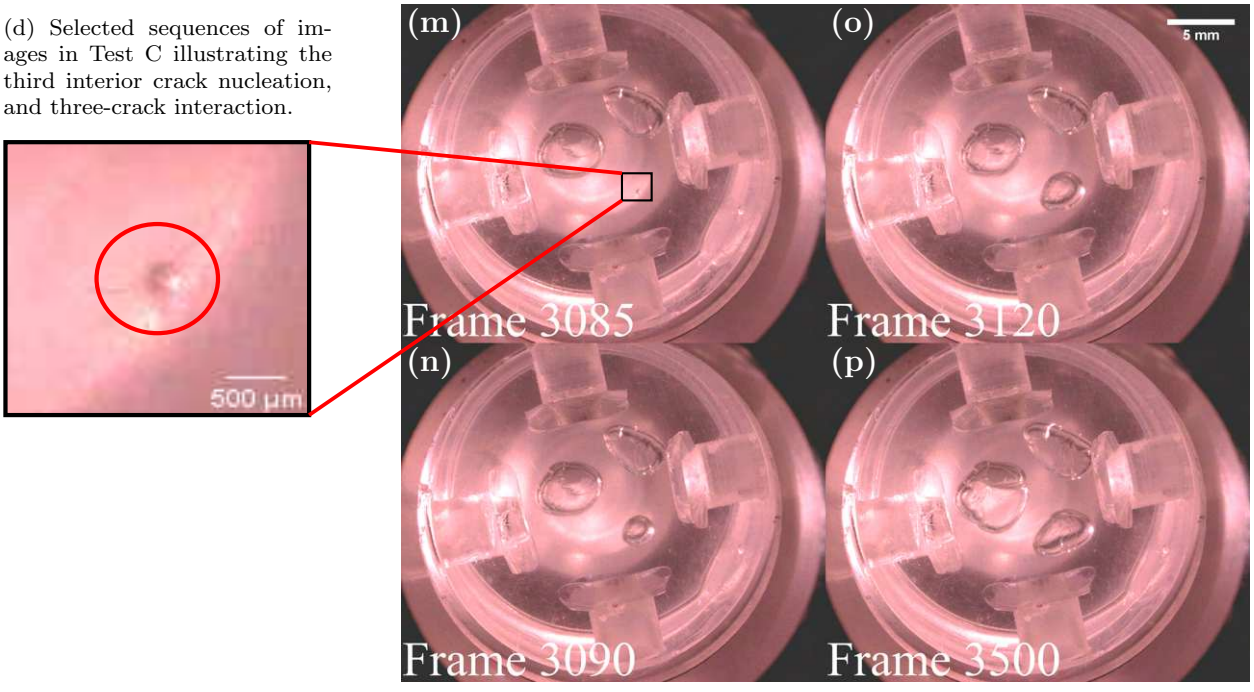

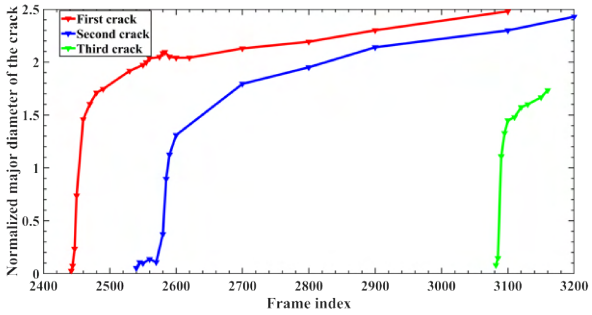

(a) Major diameter of cracks normalized by the initial thickness (Test C)

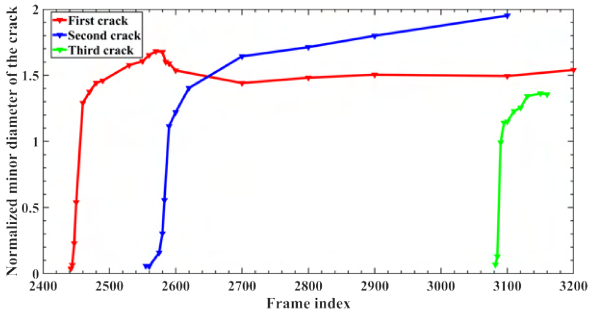

(b) Minor diameter of cracks normalized by the initial thickness (Test C)

Fig. 7: Interior crack growth rate of Test C

(configuration e) with continued growth of the interior crack to about 2 mm. At Frame 2550 (configuration f), the crack has grown to a size of 4 mm and the load dropped off significantly to $S = 0.143$ MPa, with the elliptical crack growing in the direction of the center of the specimen.

From configuration f through h, the rate of the load drop levels out as the crack continues to grow towards the center and evolves into a flat, penny-shaped crack.

The three-dimensional geometry of this macro-crack can be confirmed (through x-ray CT scan) to be a flat crack of Mode-I type, parallel to and near the rigid boundary of one of the grips. In numerous specimens with aspect ratio α in the range of 8 to 10, a similar response - dominated by the nucleation of a single defect/crack followed by (stable) growth of this crack parallel to and near one of the rigid end grips of the poker-chip specimen - was observed consistently. This response suggests that once a crack is nucleated, its subsequent growth should be governed by the Griffith criterion, but the nucleation itself may require a separate criterion.

3.3 Test C: Multiple interior crack nucleation, dominated by nucleation and growth

Next, we describe a test performed on a specimen with a thickness of 2.2 mm, corresponding to $\alpha = 11.3$, with the same experimental protocol; we label this as Test C. The normalized load as a function of time and selected microscopic images are shown in Fig. 6.

As the cross-head displacement increased, somewhere between Frame 2443 and Frame 2444 (configuration b), the first nucleation of damage formed from a location where the initial flaw was not optically detectable *a priori*, and it was already in the form of a crack with 100 μm when it first came into view, suggesting an instantaneous growth rate of ≈ 1.5 mm/s that is much faster than Test B. In contrast to Test B, structural softening was observed immediately, which is a direct consequence of the propagation of the mode I crack, as shown in the later configurations. At Frame 2450, an elliptical crack with a major axis length of 2 mm in the deformed configuration has been formed. The load continued to decrease with continued growth of the crack, but the gradient of both load decrease and crack growth is diminished with the continued stretch; in fact, the crack growth rate slows down. To see this clearly, the variation of normalized major and minor diameters of the crack with time (here identified by the frame number) is plotted in Fig. 7a and 7b, respectively. It can be seen that the first crack (red line in Fig. 7a) nucleates at frame 2444 and grows rapidly until Frame 2460 and then slows down implying that the crack is unable to extract the elastic energy from the highly constrained specimen beyond this point. Until Frame 2470 (configuration f), the *flat crack* propagates towards the center of the specimen, at a significantly slower rate. At Frame 2540 (configuration g), another crack is nucleated at a distance of about 6 mm away from the first nucleus with a corresponding load drop; magnified views of the second nucleation are highlighted in Fig. 6c. With continued loading through configurations i through l, the crack grows rapidly at first, and slowing down at about the same size as the first crack (see blue line in Fig. 7a). In fact some interaction could be observed between the two cracks: as the second crack nucleated, the minor axis of the first crack decreased slightly suggesting an elastic unloading in that direction (see Fig. 7b).

With continued loading in configurations m to p, in addition to the continued slow growth of the two previously nucleated cracks, a third crack was nucleated at a similar distance away from the previous two cracks. This crack also follows the trend of the previously nucleated cracks in growing rapidly at first, and then slowing down as it reaches a similar length; cor-

responding to this increase in compliance, there is another load drop. With further loading all three cracks exhibit stable growth under displacement control, and eventually splits the specimen into two pieces. Repeated experiments with the aspect ratio in the range of 10 to 15 exhibited a similar response. The key observation to note is that the cracks nucleated in the interior stop growing and nucleate new cracks!

3.4 Test D: Numerous interior cracks, dominated by nucleation

The last case we discuss corresponds to a specimen with an extremely thin layer (0.6 mm) of PDMS, resulting in $\alpha = 41.6$; this is labeled as Test D. The normalized load as a function of time and selected microscopic images are shown in Fig. 8.

The first crack appears between Frame 5095 and Frame 5096 (configuration b), sitting near to the top of the image, highlighted by the black square in Frame 5096 and shown at greater magnification in the left column (see Fig. 8b). The defect/crack can be identified by the bright light reflection, and is nearly 500 μm in size. From Frame 5096 to Frame 5100, a new crack was nucleated in every other frame as highlighted by the blue and green rectangles and shown at larger magnification in the left column. We emphasize again that this is the deformed configuration of a penny-shaped or elliptical interior crack, projected in 2D. Each nucleated feature is between 500 μm and 1000 μm in size, is separated from the previous nucleation by a distance of a few mm, and is clearly triggered[7] sequentially by the previously nucleated crack. Intriguingly, as the first three cracks were nucleated, the macroscopic load on the specimen, continued to increase, albeit at a slower rate, as seen from the inset in Fig. 8a.

With continued stretching at the same rate, a *set* of 7 cracks were nucleated within the 67 ms time interval between Frames 5100 (configuration f) and 5101 (configuration g) (see Fig. 8c). Since the size and spacing between the nucleated cracks resemble the first three nucleation events, we infer that this is also a sequential nucleation of similar origin. This process continues with the sequential nucleation seen in Frames 5102 (configuration h), 5110 (configuration i) and 5115 (configuration j). In all these cases, cracks nucleate, but are unable to grow beyond a certain size of the order of the thickness of the specimen, and they trigger nucleation of another crack in the vicinity. It is also noted that at configuration j, the macroscopic load begins to drop significantly, indicating that the cracks developed so far have significantly increased the compliance of the specimen.

Selected sequence of images for configurations k through p are shown in Fig. 8d. In Frame 5150 (configuration k), there are $\mathcal{O}(10^2)$ nucleated cracks pervading the cross-section; clearly, the growth of the nucleated cavities is resisted by the birth of the surrounding cracks. It is only after the entire cross-section is covered with nucleated cracks, do they begin the growth phase as shown in Frames 5200 and beyond. During this time, the existing cracks propagate, and the inter-region between each crack is being contracted in the transverse direction and stretched in the axial direction, and eventually becomes a thin film or fibril, with the entire cross-section resembling a honeycomb structure.

Eventually, the individual cracks coalesce with each other and separate the specimen into two pieces. Coalescence of these cracks begins at configuration p and continues beyond.

Repeated tests with specimens with aspect ratio between 40 and 75 indicated a very repeatable nucleation dominant response described in this section. The primary conclusion is that in this range of aspect ratios, nucleated cracks are unable to grow beyond a certain size, but nucleation of new cracks in the vicinity dominates the response!

4 Nucleation and growth of cracks under *triaxial* loading: x-ray computed tomography observations

In this section, we explore the three-dimensional geometrical aspects of the nucleated interior cracks and their further growth, with the aim of addressing the following questions: (i) where does the crack initiate in the poker-chip specimens; (ii) what is the geometry of an isolated crack just after nucleation, and (iii) how does the crack propagate to dimensions comparable to the diameter of the poker-chip specimen. These experiments were performed with Apparatus B (see Fig. 3) following the experimental protocol described in Sec. 2. In addition, the x-ray related parameters are set as in Table. 2.

[7] Since the central region is under a nearly uniform stress state, random nucleation is expected from the weakest point for the first crack. However, the next crack is nucleated, almost always, in the vicinity of the previously nucleated crack - not from the next weakest point globally, but from the weakest point in the neighborhood of the first crack; this is why we refer to the subsequent cracks being "triggered" by the previously nucleated cracks. The nucleation of the first crack causes the stress in the vicinity to drop (due to the increase in the local compliance of the specimen), and shields a certain region from further nucleation; but it must also elevate the stress beyond the region and cause the second nucleation.

Fig. 8: Test D, numerous interior crack nucleation

(a) Normalized force versus time in Test D with $\alpha = 41.6$

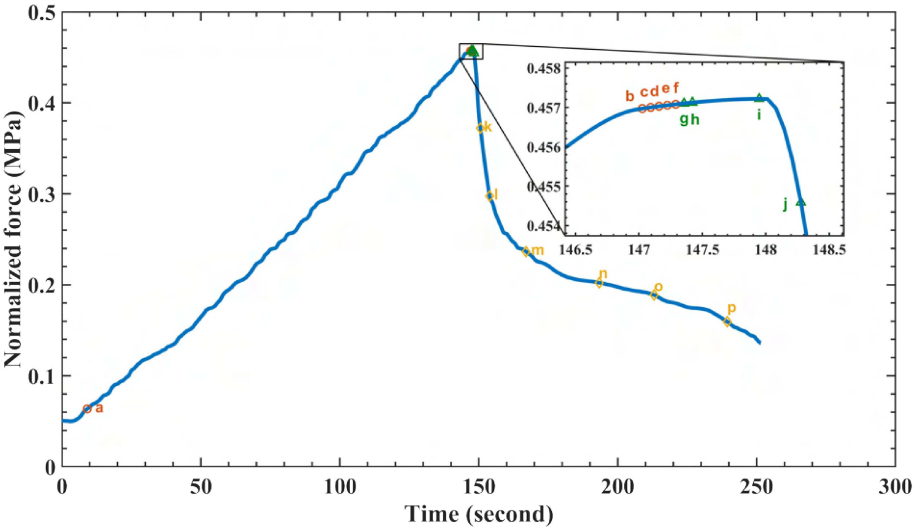

(b) Selected sequences of images in Test D illustrating the interior sequential nucleation before the mechanical instability

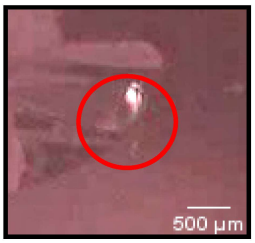

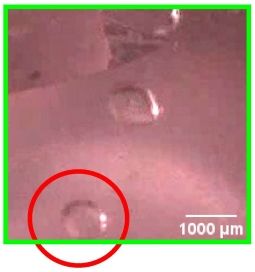

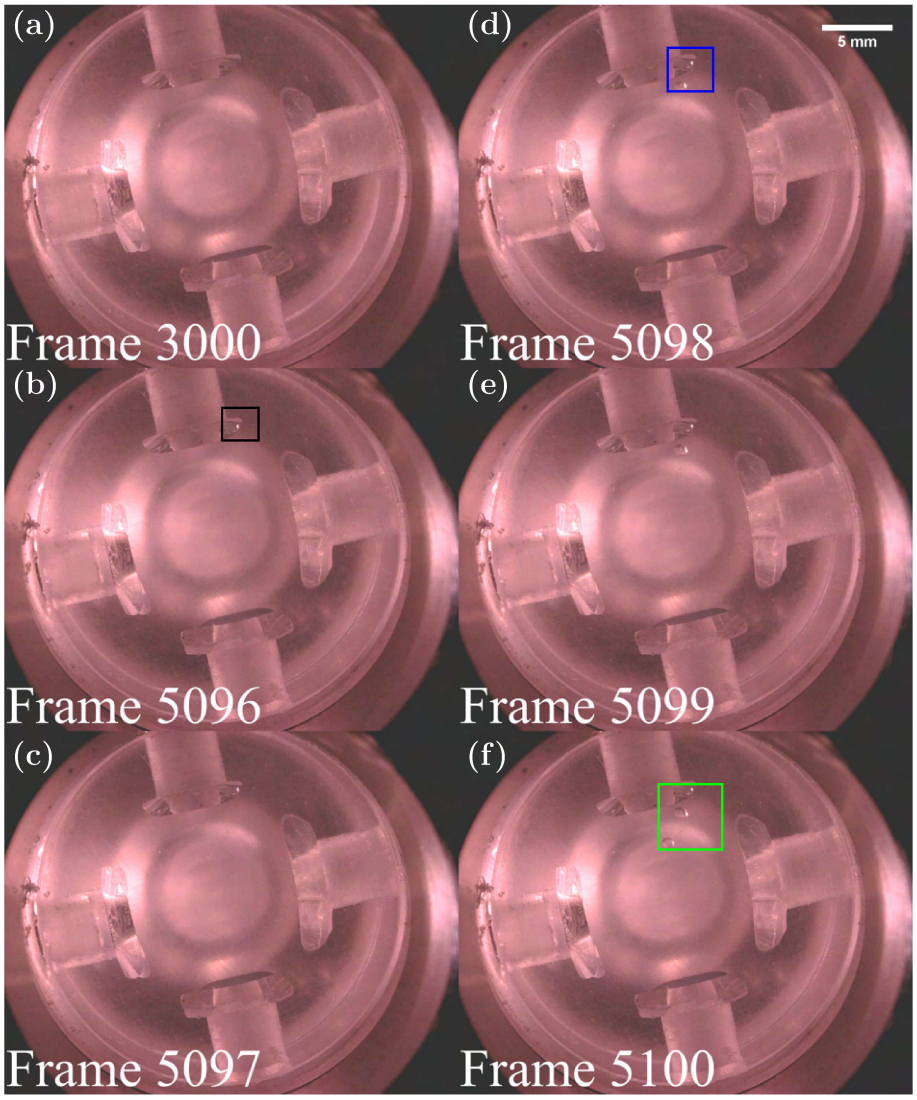

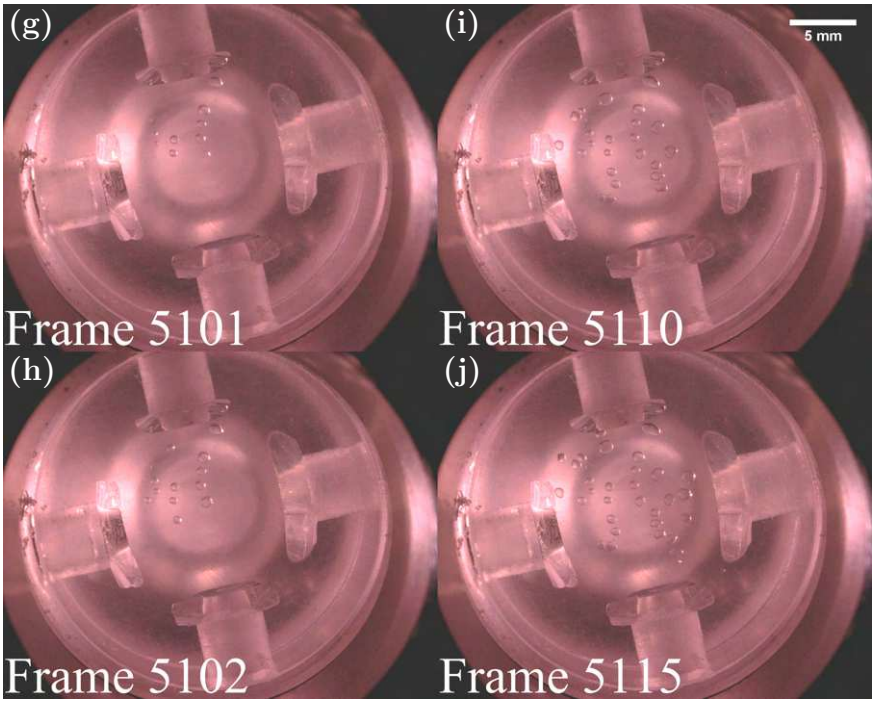

(c) Selected sequences of images in Test D illustrating the interior sequential nucleation after the mechanical instability

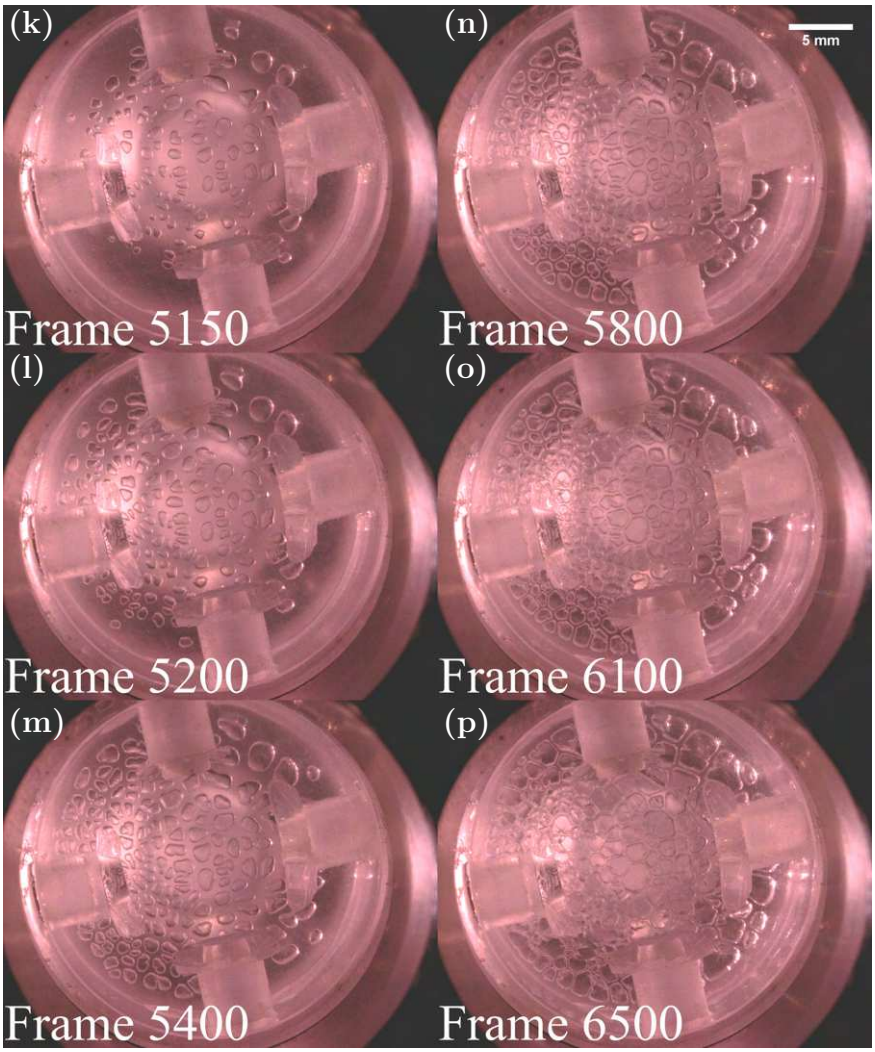

(d) Selected sequences of images in Test D illustrating the interior crack growth and coalescence

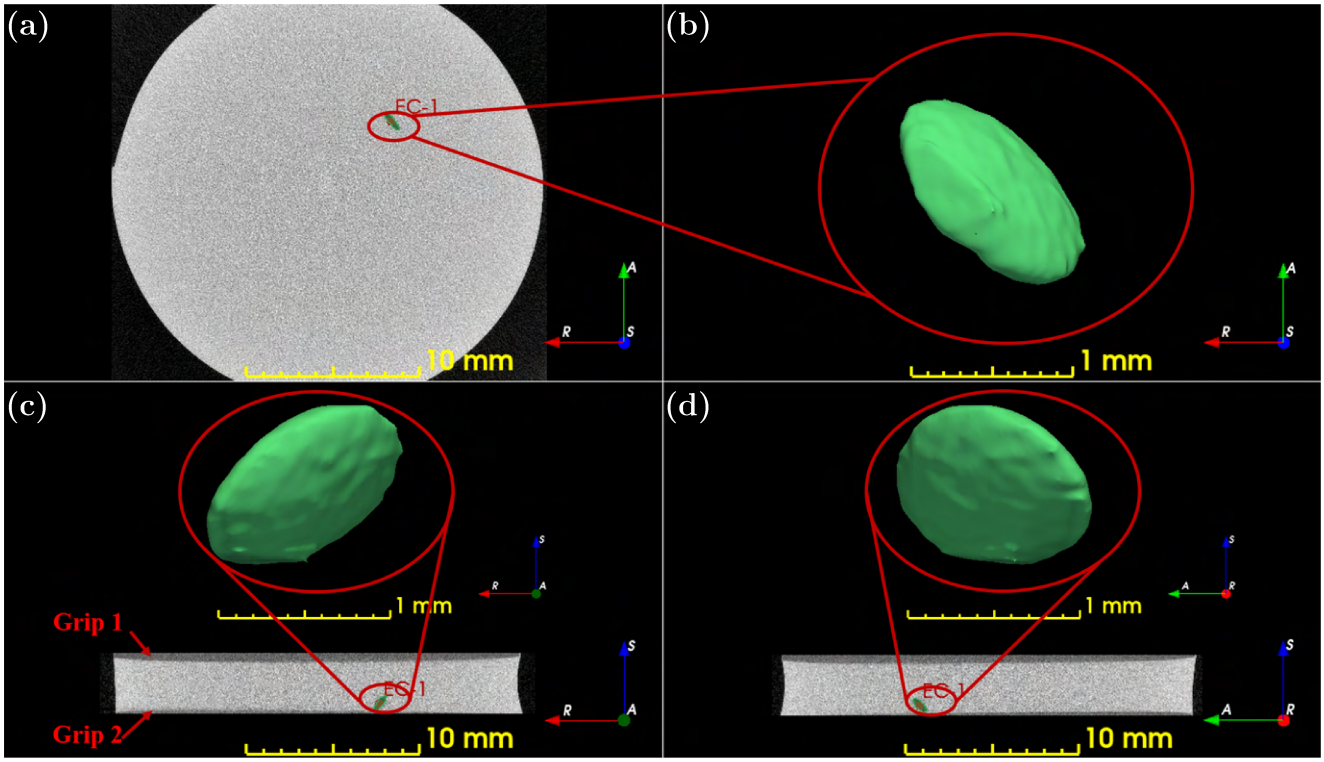

Fig. 9: EC-1 is the first nucleated crack of Test E (current thickness $T = 3.1$ mm), that at this configuration is about 1 mm in major dimension, located near to the bottom boundary with a slanted minor principal axis relative to the axis of the specimen.

X-ray tube voltage	70 kV
Current	114 μA
Scan time	30 ∼90 min
resolution	10 μm / pixel

Table 2: X-ray micro-tomography parameters

4.1 Tests E, F, G and H

Test E corresponds to a poker chip specimen with an aspect ratio $\alpha = 8.2$; the specimen was mounted in Apparatus B and loaded manually in small increments until the first nucleation was observed visually; the load was then swiftly decreased in an attempt to freeze the crack at the nucleation stage; the specimen, still in the loading frame, was then placed in the x-ray scanner and a 3D image was acquired; a single crack was identified, but this crack had already grown to about 1 mm in size and hence is not at the initiation stage. This crack, identified as crack EC-1 is shown in a 3D rendering in Fig. 9. In this figure, the gray-scale section views correspond to the reconstructed tomographic image slices, where the RAS coordinate on the right below indicates the orientation of each projection. Materials of different densities are discernible based on the different intensity of pixels; in this figure for instance, black pixels denote voids, dark-gray and light-gray pixels denote the grips and PDMS elastomer, respectively. In order to depict the geometry of the crack, magnified views of each crack with the same projection are inserted in the figure. Moreover, we fit the crack profile with an ellipsoid to convey quantitatively the geometric information, such as the location of each crack identified by the centroid of the ellipsoid, and the orientation of the crack, represented by the principal axis. We note that the crack has already grown to about 1 mm in major dimension, it is slanted relative to the axis of the cylindrical specimen and its centroid is close to the bottom rigid grip.

The specimen was then removed from the x-ray scanner and loaded further to continue the growth of crack EC-1; the loading was stopped when a second crack, EC-2, was nucleated. Three-dimensional images of both cracks EC-1 and EC-2 were obtained using x-ray CT scan and are shown in Figs. 11 and 10, respectively. The nucleation of crack EC-2 was captured when this crack was only about 200 μm in size; it reveals features similar to crack EC-1 at the earlier loading stage, in that it is close to the bottom rigid grip, appears to be ellipsoidal, but less slanted relative to the axis of the cylin-

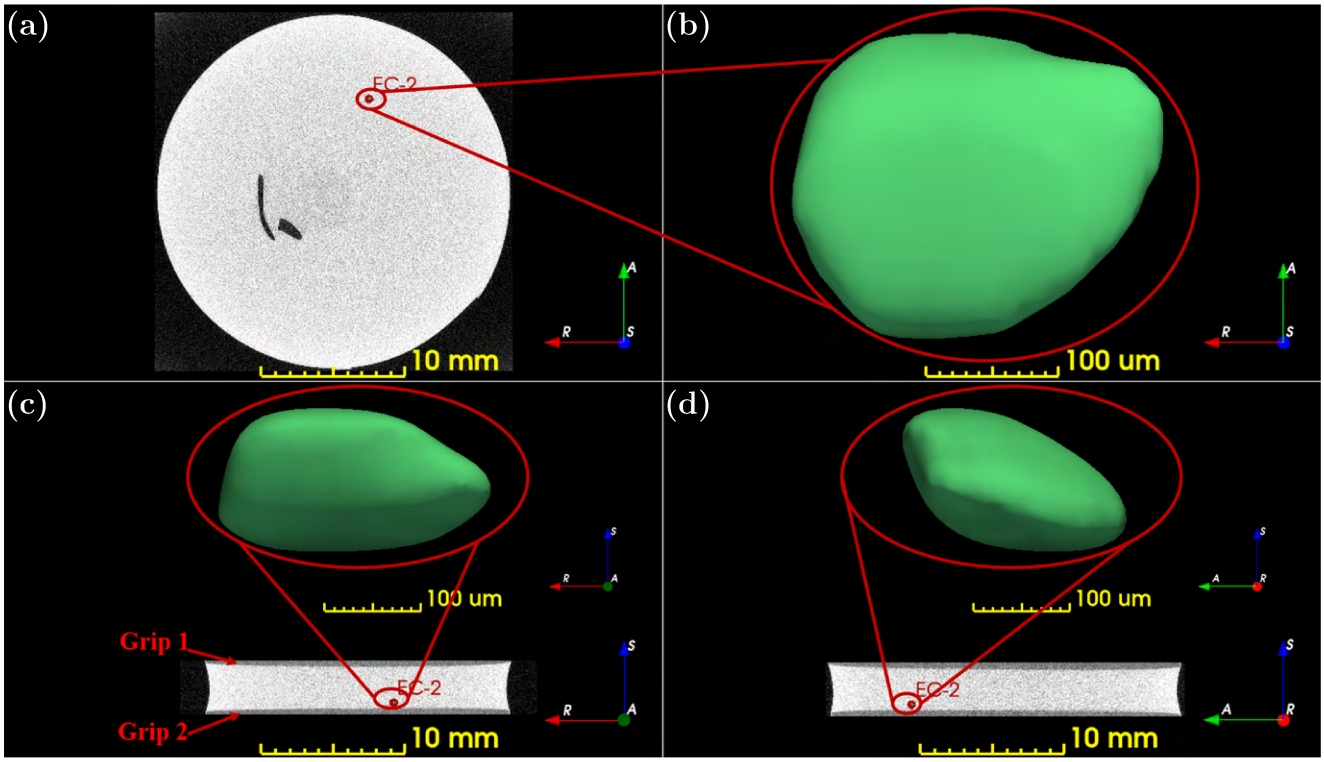

Fig. 10: The second configuration in Test E (thickness $T = 3.1$ mm) representing the centroid location and cross-section of the second crack, named as EC-2. The green ellipsoid is the magnified view of EC-2, about 200 micron in major diameter, and inclined to the bottom boundary of the specimen

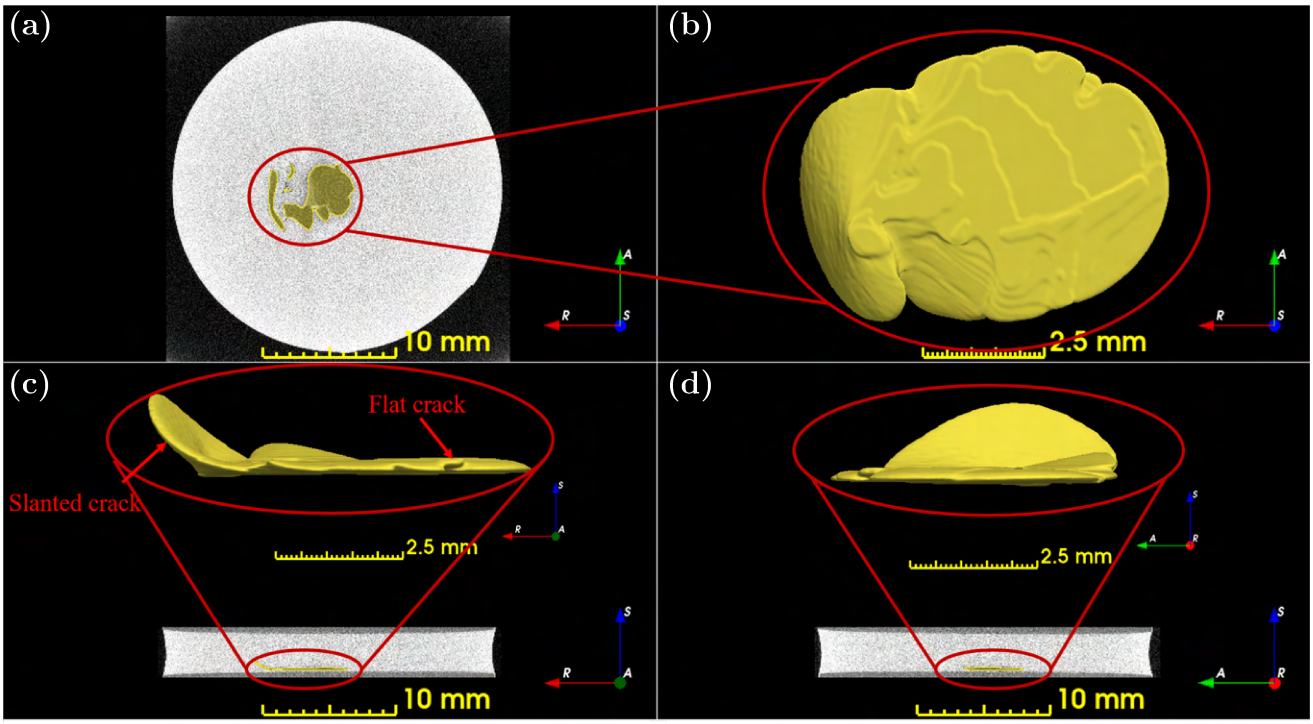

Fig. 11: The further growth of the first crack EC-1 in Test E. A flat crack parallel to the rigid plane emerges from the bottom end of the slanted crack, while the top crack front continues to grow in the same tilted direction.

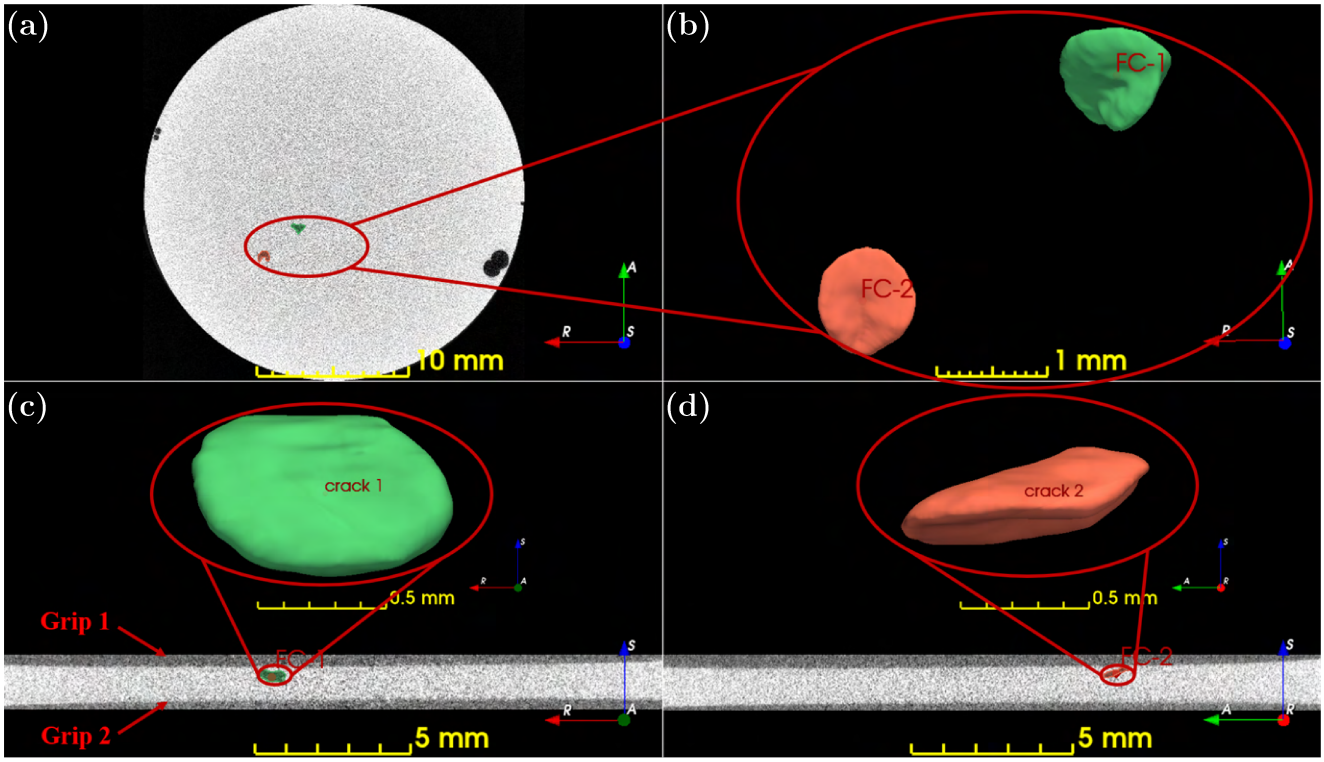

Fig. 12: The first configuration of Test F (thickness $T = 1.36$ mm), showing two independent cracks FC-1 and FC-2 that are simultaneously nucleated, while the two bottom subfigures denote the slice views across the centroid of each crack that sits near to the top boundary, rendered as green and orange ellipsoids in the magnified views

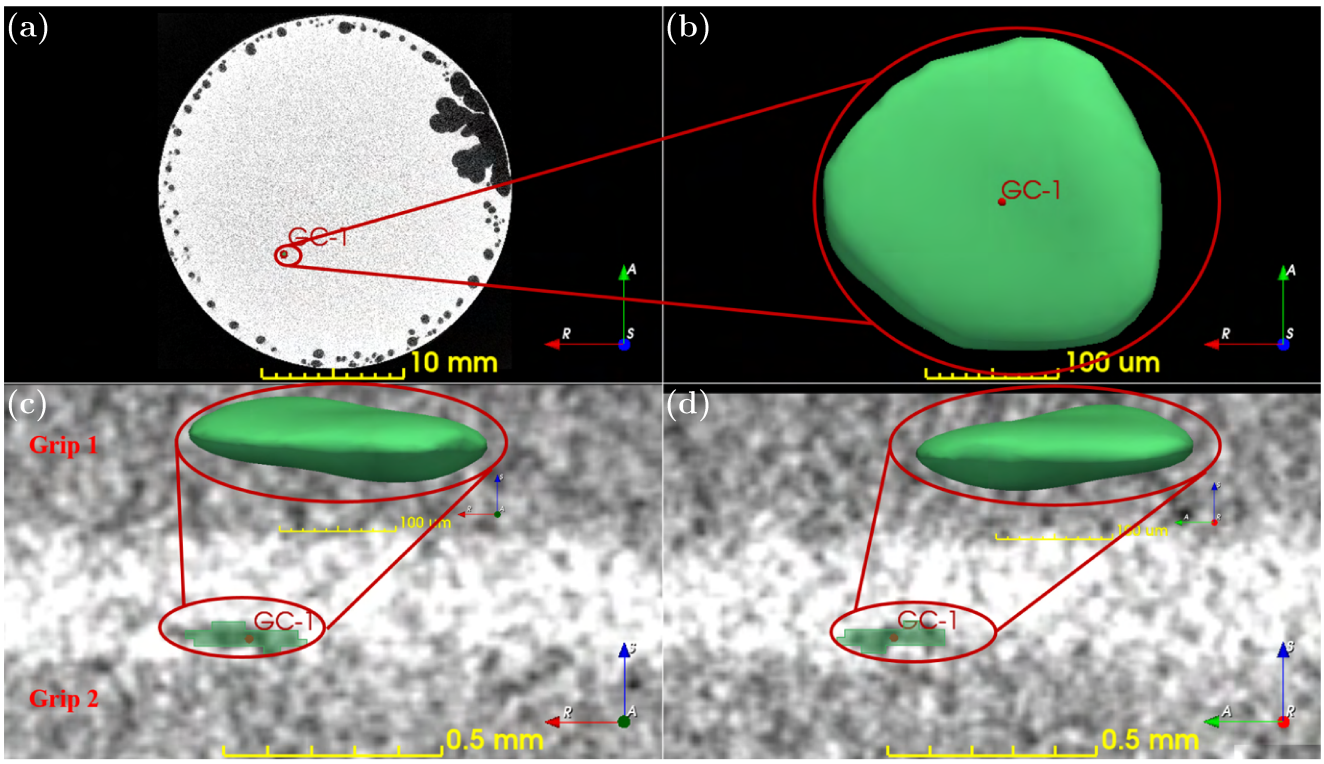

Fig. 13: The first configuration of Test G (thickness $T = 0.33$ mm), with two enlarged side views. Crack GC-1 as the first nucleated crack of around 200 μm in major dimension is evidently slanted to the bottom boundary

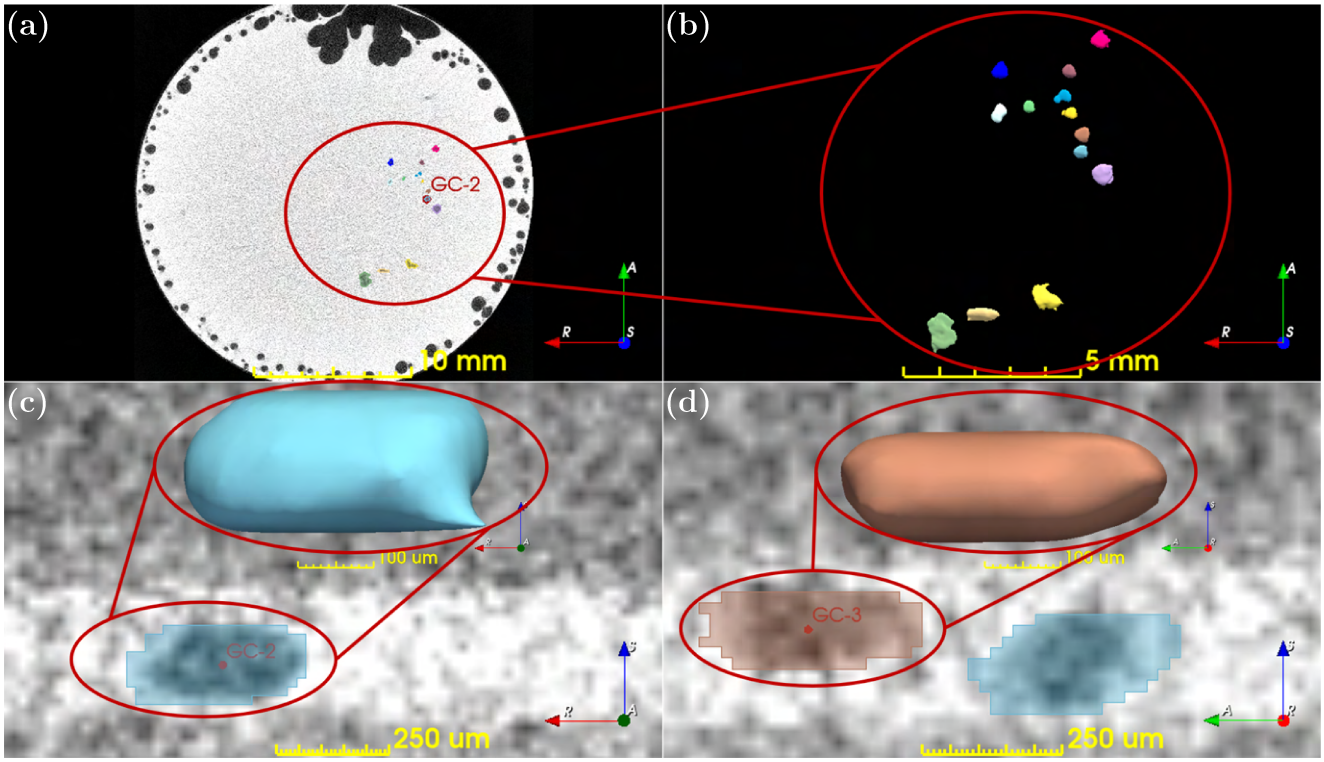

Fig. 14: The further loading state of Test G, where it includes 13 independent cracks according to the top view; only two of them (GC-2 and GC-3) are selected for a magnification in the side view, i.e. the cyan and brown segments, that are comparable to the thickness.

drical specimen. The continued growth of crack EC-1 exhibits additional interesting features as indicated in Fig. 11. First, there is a large crack (about 5 mm in major dimension) that is very nearly flat and has grown parallel to and close to the rigid end grip. Second, there is a slanted crack at one end of the flat crack. From a comparison of the two sets of x-ray images at increasing load levels, it is clear that the flat part is due to the continued growth of the earlier slanted appearance of EC-1. Third, the crack front exhibits fragmentation (discontinuities) that are indicative of the formation of echelon cracks under mixed-mode I + III loading (see Baumberger et al. (2008), Pham and Ravi-Chandar (2017)).

Tests F and G focus on the influence of the specimen aspect ratio on the nucleation of cracks (see Figs 12, 13 and 14. Two nucleation events were captured in Test F with $\alpha = 18.4$. These cracks exhibit features similar to that identified for crack EC-2 in Test E. Test G with $\alpha = 75.7$ falls in the range where nucleation dominated over growth and hence these cracks did not grow much. In this test, the first observation indicated a single nucleation (see Fig. 13); when loaded further, this triggered a few more nucleation events from the first crack, as well as a cluster of ten additional nucleation events from a different location (see Fig. 14 as a schematic); as with the observations on Test E, nucleation occurred close to one of the rigid end grips.

Growth of the cracks beyond the early stages was examined in Test H, with aspect ratio $\alpha = 10.2$ that was loaded significantly beyond the onset of initial damage. The 3D geometry of the cracks is shown in Fig. 15. A single slanted crack cuts across the diameter of the specimen; where the slanted cracks approach the rigid grip surfaces, the cracks kink and grow nominally parallel to the rigid end grips. However, at a smaller length scale, these crack fronts fragment due to a mixed mode loading, as can be seen from the 3D perspective rendition in Fig. 15b. The corresponding optical microscopic image is shown in Fig. 16.

5 How do silicone poker-chip specimens fail?

From the collection of optical and x-ray observations described above we get a clear picture of what happens during deformation and failure of the poker chip specimens. In this section, we summarize the process of failure in the poker chip specimens of PDMS. We note that this elastomer does not exhibit strain-induced crystallization and may present quantitative differences from

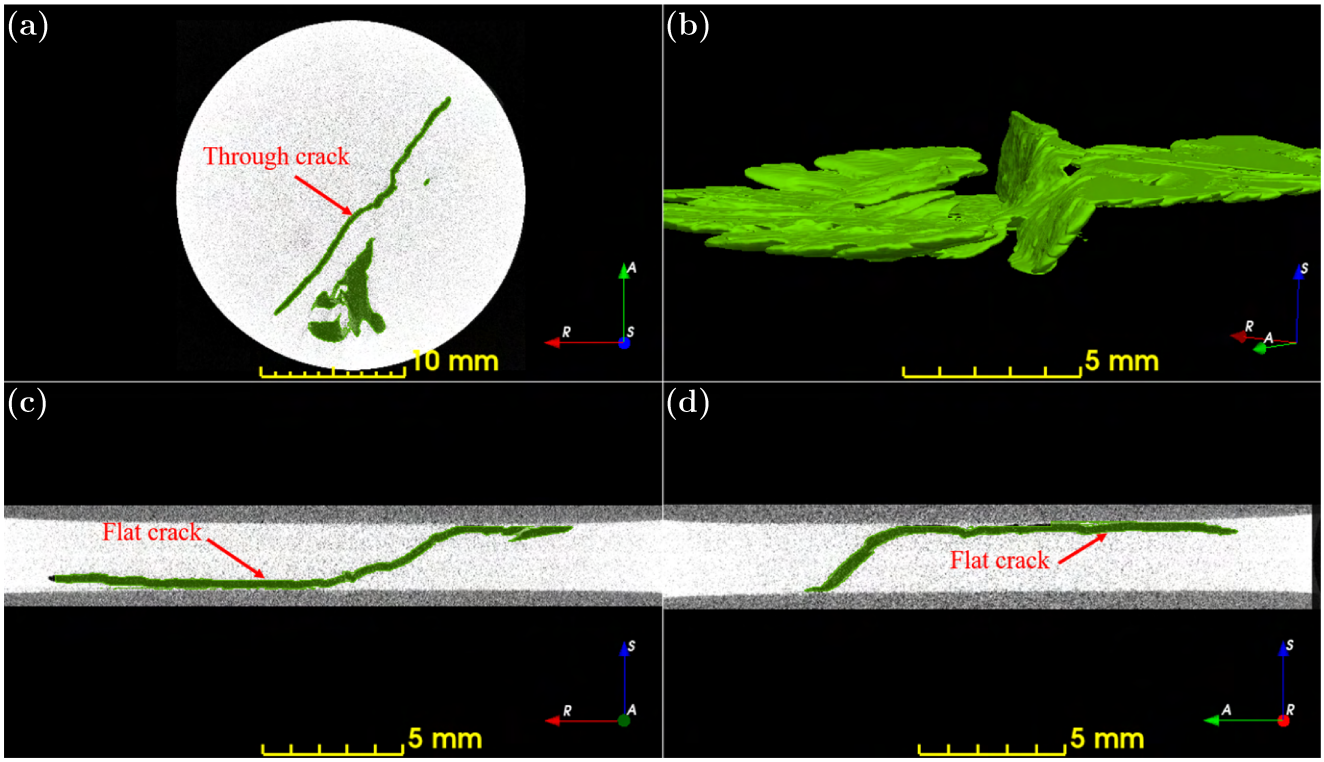

Fig. 15: Test H (current thickness $T = 2.45$ mm) includes a single crack that pervades the entire domain of the specimen; the volume rendering shows the crack is a combination of a through crack across the radial direction, and two flat crack adjacent to the two rigid boundaries respectively; moreover, the fragmentation in lower length scale due to mixed-mode loading experienced.

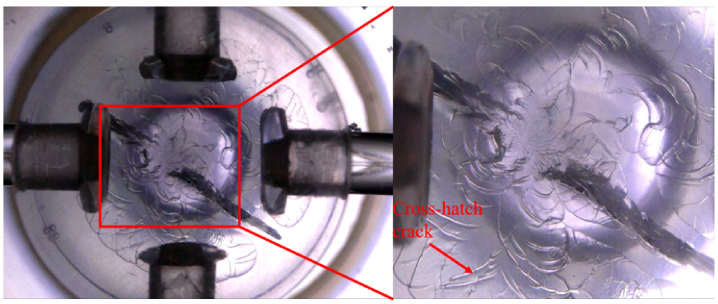

(a) Cross-hatch crack

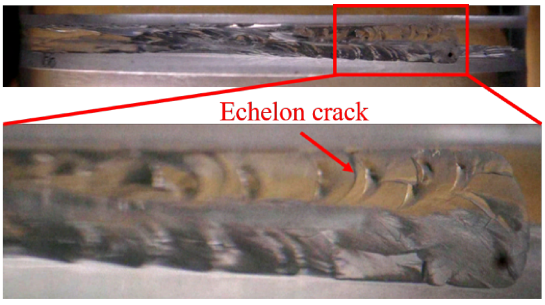

(b) Échelon crack

Fig. 16: (a) Snapshot of the microscopic image of the top view of Test H, where the cross-hatch pattern is triggered during the flat crack propagation; (b) Snapshot of the microscopic image of the side view of Test H, where the échelon crack instability is evident during the through crack propagation.

natural rubber considered by Gent and Lindley (1959).

5.1 Crack nucleation under *triaxial* loading state

It is evident that the response is correlated with the aspect ratio, α, and therefore we explore a range of aspect ratios $\alpha \in (2, 75)$, from which the nucleation and growth characteristics of the cracks and the critical mechanical response can be determined. Images of fracture patterns from a selected set of experiments at different aspect ratios in this interval are shown in Fig. 17. Pictorially, the diagram delivers a message that, as the geometric confinement increases, the fracture nucleation transits from surface nucleation, to interior nucleation that is dominated by growth, and eventually to

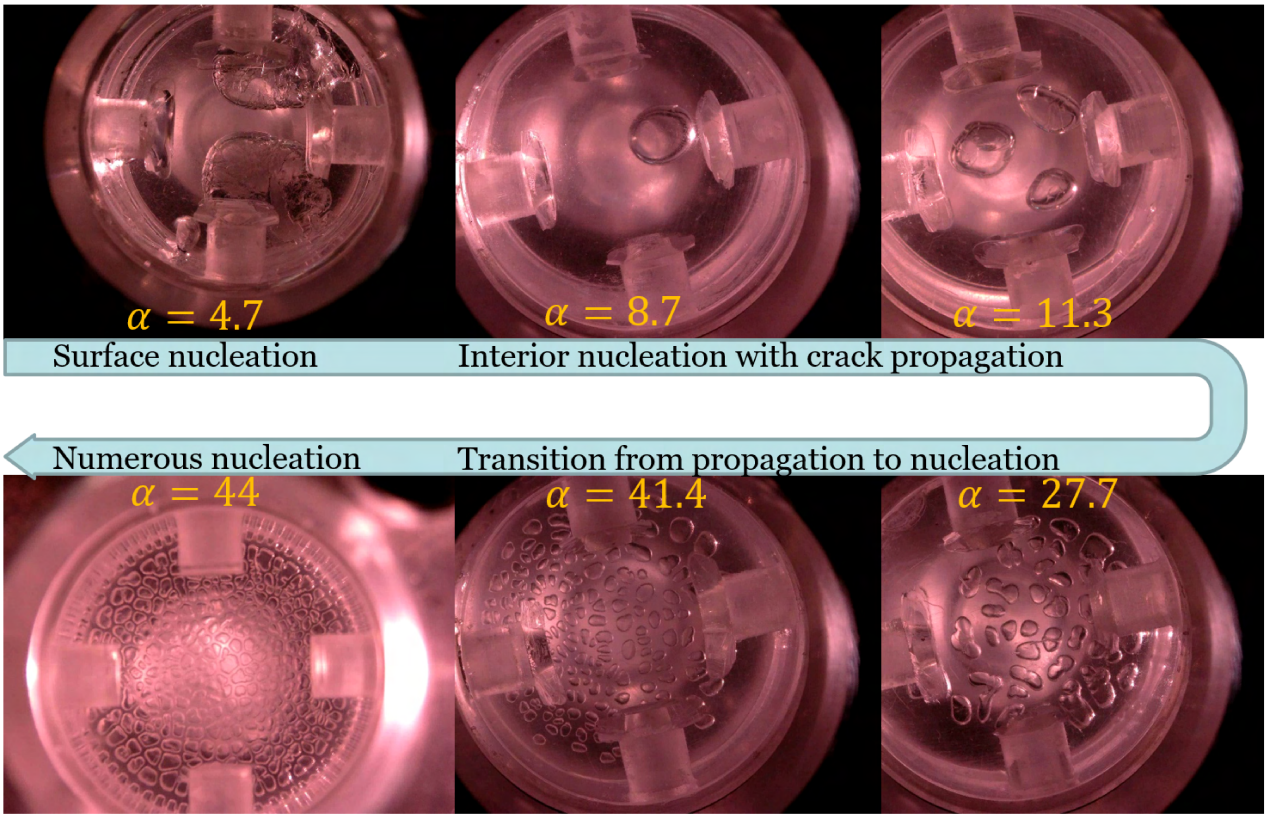

Fig. 17: Progression of fracture events in the poker-chip test with specimens of six different aspect-ratios.

the interior nucleation-dominated scenario with limited growth.

Clearly, nucleation of a surface crack occurs first, when $\alpha < 5$, perhaps from defects that are below the visible limit. The axial location is close to one of the end grips, and is attributed to a stress concentration in this region. The hydrostatic tension in the interior of the specimen is relatively low in this specimen and hence nucleation in the interior is not observed. Subsequent growth of the nucleated crack is expected to be governed by Griffith energy balance. Nucleation of more than one surface crack has also been observed in some of these experiments; this could be attributed to a distribution of strength controlling defects in the specimen. Analysis of this problem requires calibration of material strength to capture the surface nucleation, and a fracture energy to capture the growth. While the latter is accomplished using the tools of fracture mechanics, the former is influenced by surface flaws and subject to large scatter. Nevertheless, the experimental measurements can provide an estimate of the surface strength as will be discussed in Sect. 6.

For $\alpha \in (5, 40)$, large hydrostatic tensile stresses develop in the interior regions of the specimen and crack nucleation occurs in these interior regions, with the optical and x-ray images confirming that these cracks are indeed nucleated away from the rigid end grip planes as well as the free surface of the specimen; they are neither adhesive failure nor surface defect triggered failure. The location and geometry of the nucleated cracks will be discussed in Sect. 6. The number of nucleated cracks and their subsequent growth depend crucially on the aspect ratio α. It is clear from Fig. 17 that the larger is α, the greater is the number of independent cracks that are nucleated.

For $\alpha \in (8, 10)$, a single nucleation occurs, followed by the growth of this crack under continued displacement of the end grips. This is expected since the hydrostatic tensile stress is expected to decrease throughout the entire domain upon first nucleation, and prevent further nucleation. As α is increased further to the range of 10 - 15, an interior crack is nucleated at a critical load; this crack grows initially, but quickly slows down because it is unable to extract the elastic energy from the highly constrained specimen beyond a certain amount of crack growth; however, the hydrostatic tensile stress and the elastic energy in the regions beyond the first crack are still large enough to trigger nucleation of another crack that a second crack is nucleated at some distance from the first crack; nucleation of the

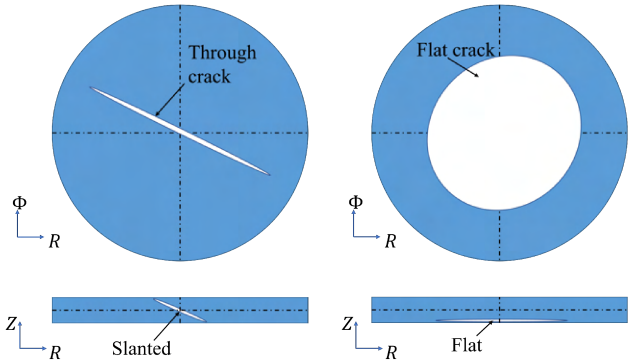

Fig. 18: Schematics of the through crack and flat crack

second crack results in a slowing down and/or unloading of the first crack. For the specimen with aspect ratio of 11.3, three nucleation and growth events were observed. Eventually, these cracks will interact with each other and break the specimen into two pieces.

For $\alpha > 40$, the specimen is extremely thin and develops a very high hydrostatic tensile stress but very little elastic energy. While the first nucleation of an interior crack still resembles that at lower aspect ratio specimens, albeit nucleated at greater stress levels, the nucleated crack is unable to grow beyond a length of about one specimen thickness; however, since the hydrostatic tension in regions away from the previously nucleated crack is still large, a new crack nucleates - indeed a cascade of new cracks may nucleate; furthermore, they occur sequentially and in spurts with each crack unable to grow beyond about one thickness as shown in Fig. 17 and in the Supplementary Video of Test D.

In summary, this indicates a transition in the cracking behavior with aspect ratio: (i) surface crack nucleation and growth; (ii) interior nucleation and growth of cracks; (iii) primarily interior nucleation without significant growth. That is, if the specimen is extremely thin, once the nucleation is triggered, the local strain energy is not large enough to continue further crack growth, but the re-distributed stress field is still large enough to promote other nucleation in the surrounding area. In the following, we conduct image analysis to determine the geometrical features and spatial distribution of the nucleated cracks and the growing cracks.

5.2 Crack propagation under *triaxial* loading state

In addition to the continuous opening of the first nucleated penny-shaped or ellipsoidal crack, the crack geometry evolves during continued growth. From the post-mortem figures of Gent and Lindley (1959), it is commonly believed that the nucleated crack turned into a penny-shaped crack across the radial direction of the thicker specimens; later in the work of Lindsey et al. (1963) with the investigation of transparent polyurethane rubber, the authors observed the slanted and flat shaped cracks. These observations from the earlier work are correct, but not complete, since all these cracks are possible, and are formed in a sequential manner. From our extensive set of experiments, by and large, the crack growth mode falls into three classes; these are described below.

- Cracks that are slanted with respect to the loading direction: The slanted crack is a continuation of the initiated crack, with the corresponding major dimension of crack in the same orientation.
- Cracks that are flat and parallel to the rigid boundary: In addition to the continued opening/growth of the nucleated slant crack, a flat crack usually occurs at the crack front of the slanted crack that is close to the rigid boundary, without forming interfacial delamination (see the flat cracks in Fig. 11 and Fig. 15, as well as the schematic in Fig. 18).
- Cracks defined as through cracks that propagate along the radial direction: On top of the flat crack, the slanted crack grows along the radial direction, such that the crack size in the radial direction is larger than the slanted direction, as indicated in Fig. 15; we refer to this as a "through-crack", as depicted in Fig. 18.

The growth of these cracks is expected to be governed by the Griffith fracture theory, but simulations are made difficult mainly by the rearrangement of the local triaxial stress field associated with the complex crack geometry. As can be seen from Fig. 16, development of the cross-hatch instability on the flat crack (Baumberger et al. (2008)), and échelon crack on under mixed mode loading (Pham and Ravi-Chandar (2017)) introduce difficulties in modeling growth of cracks in the poker chip specimen.

The above classification of crack growth applies *only* to specimens of small aspect ratios where a few cracks nucleate; for specimens with aspect ratio greater than about 40, where nucleation is dominant, each nucleus only grows into an oblate ellipsoid until the entire specimen is filled with such nucleated cracks, see Fig. 14. The growth and coalescence of the multiple cracks in large aspect ratio specimens is much more complex and requires further investigation.

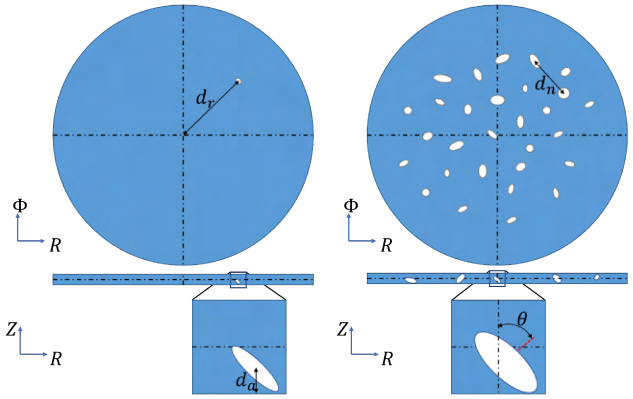

Fig. 19: Geometric measure of interior nucleated cracks in two-dimensional projection: d_r denotes the distance from the centroid of the *first* nucleated crack to the specimen radial center; d_a denotes the closest distance from crack centroids to the rigid boundary; d_n represents the interdistance of each crack; θ represents the tilted angle of a crack w.r.t. the specimen axis

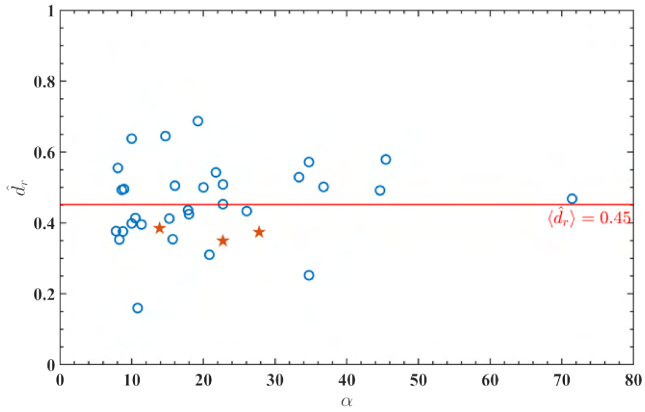

Fig. 20: Normalized distance from the centroid of crack to radial center $\hat{d}_r$. Circle markers represent the collected $\hat{d}_r$ based on different aspect ratio

6 Quantification of the 2D and 3D observations

We now turn to quantification of the geometric characteristics of the nucleated and growing cracks based on the optical and x-ray imaging. We also discuss the macroscopic loading corresponding to nucleation of cracks.

6.1 The location of the first crack nucleus in the radial direction

Nucleation of the first crack in the poker-chip experiments is identified from the video images when the crack size is about 0.1 mm; the radial distance from the center of the poker chip specimen to the nucleus of the crack is measured. We denote this distance, normalized by the initial radius of the poker chip, as $\hat{d}_r$ (see the diagram in Fig. 19); The collection of $\hat{d}_r$ from numerous tests for different aspect ratios is plotted in Fig. 20. There is quite a large scatter in the radial position at which the first nucleation occurs; this scatter may be attributed to the random distribution of crack nucleating defects in the PDMS. More interestingly, the first nucleation does not occur within the center of the poker-chip specimen; since this is the location with the largest hydrostatic tension, it is commonly assumed to be the location of nucleation in the literature. However, Lindsey et al. (1963) and Euchler et al. (2020) observed a similar nucleation-free central zone; Lindsey et al. (1963) identified that nucleation occurred at $0.4R$, but suggested that this could be due to bending influence in the loading system, dependent on the degree of misalignment and the Poisson's ratio (incompressibility). We performed finite element simulations of a misaligned poker chip specimen and found very little influence on the stress state for anticipated amount of misalignment. Moreover, x-ray images in the loaded configuration indicate little bending. In order to definitively exclude the effect of bending, we repeated the experiments, but this time with a polycarbonate sleeve restricting the movement across the rigid end grips of the poker-chip specimen to be purely axial; any bending due to specimen misalignment would be carried by the sleeve and not influence the poker-chip specimen. The first nucleation was still away from the center of the poker chip; the corresponding results are shown by the red pentagram symbols in Fig. 20 and are seen to follow the trend already established.

The average of $\hat{d}_r$ turns out to be $\langle \hat{d}_r \rangle = 0.45$, implying that the first interior crack may nucleate at almost half of the radius from the center of the specimen. *Clearly, nucleation of the crack does not occur in the center of the poker-chip specimen*, the region with the largest hydrostatic tensile stress. Therefore, the nucleation criterion must involve not just the mean stress, but perhaps also the other components of the stress tensor as well as the strain energy in the system.

6.2 The location of the first crack nucleus in the axial direction

With the help of the x-ray scan, the spatial distribution of the interior crack is resolved further to an additional dimension, i.e. the axial direction. It was widely believed that cavitation nucleates along the mid-plane of the poker-chip geometry; this is because although the

largest hydrostatic stress occurs at the intersection of rigid end grip and central axis, the largest deformation occurs at the intersection of the mid-plane with the central axis (see more discussions in Fond (2001)). But this is clearly contradicted by our x-ray images which indicate that the interior cracks seem to occur always at a location near the rigid boundary; the recent results in Kumar and Lopez-Pamies (2021) point to possible nucleation away from the boundary.

To locate quantitatively the position of the nuclei, the normalized distance between the centroid of the nucleus and the nearest rigid boundary, denoted by $\hat{d}_a := d_a/T$ (see Fig. 18), is determined for each available crack at the configuration where the size of cracks is one order of magnitude less than the corresponding specimen thickness. Based on the assumption of isotropic growth of the of crack at its nucleation, we presume the crack nucleus to be at the centroid of the ellipsoidal (or penny-shaped) crack. But the quantitative measure could be refined further if the test apparatus enables one to capture the very beginning of the burst, while the crack size is still in the sub-micron scale. We note that the present estimate of the crack location provides an upper bound for the distance in cases where the crack growth is preferentially towards the interior of the specimen. Data on the crack location $\hat{d}_a$ from a collection of seven nucleated cracks is included in Fig. 21; the normalized nucleation distance appears to be $\langle \hat{d}_a \rangle = 0.2$ in average, independent of the aspect ratio. This would imply that nucleation is governed not only by the pressure field and potential void in sub-micron or nano scale as discussed extensively in the literature, but by an intrinsic nucleation criterion. Kumar and Lopez-Pamies (2021) have proposed a strength-based criterion; we will explore the calibration and implementation of this criterion in Part II.

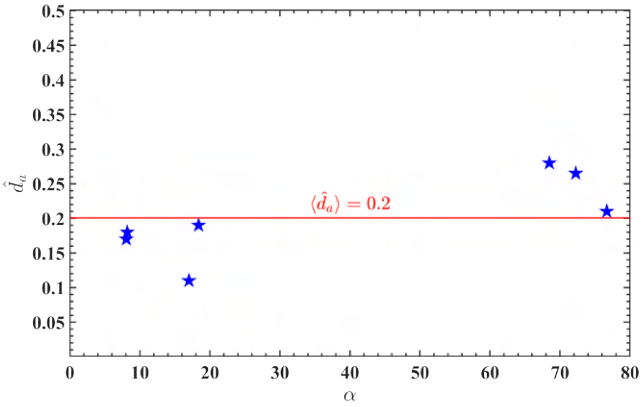

Fig. 21: Normalized distance from the centroid of crack to rigid boundary $\hat{d}_a$. Blue pentagram markers represent the collected $\hat{d}_a$ based on different aspect ratio.

6.3 Orientation of the penny-shaped crack

Even though the location of the crack nucleation is independent of the specimen aspect ratio as discussed above, continued crack growth is significantly influenced by the aspect ratio. This observation is well-captured by the cracks in Tests E and G, when the crack sizes are comparable to the specimen thickness.

Crack EC-1 in Fig. 9, the first nucleated crack in Test E with $\alpha = 8.2$, has grown to a size of 1 mm, compared to the smaller crack EC-2; however, not only are they located at the same distance from the rigid boundary, $\hat{d}_a = 0.18$ for EC-1 and $\hat{d}_a = 0.17$ for EC-2, but they both exhibit a slanted orientation from the central axis. By orientation, we refer to the orientation of the minor principal axis of the fitted ellipsoid relative to the axis of the poker-chip specimen, see the schematic in Fig. 19. Hence, one obtains the tilted angle $\theta = 57.7°$ for EC-1 and $\theta = 31.7°$ for EC-2.

In contrast, for the nucleation dominated cracks in Test G (aspect ratio $\alpha = 72.2$) in Fig. 14, their crack orientation is nearly parallel to the axis of the poker-chip specimen, with an average tilt angle of $\theta = 2.5°$.

The tilt angle of the cracks for three different aspect ratios is summarized in Table. 3, from which one might claim that the fracture surface tends to be more parallel to the base of the cylinder with decreasing thickness, but this requires significantly more data to confirm.

Aspect ratio	Principal axis	Tilted angle (°)
8.2	(0.654, -0.535, 0.533)	57.7
18.4	(-0.183, 0.496, 0.848)	32.0
72.2	(0.024, -0.007, -0.999)	2.5

Table 3: Minor principal axis of the ellipsoidal cracks for specimens of different aspect ratio

6.4 Spatial distribution of the crack nuclei

The critical state for nucleation of cracks is dictated by the local stress and strain field, and the initial defect distribution; however, the inner traction-free boundaries created by the first nucleation alters the surrounding stress and deformation fields significantly, leading to the satisfaction of the nucleation criterion in its neighborhood. This rearrangement dictates the interdistance between neighboring crack nuclei. In this section, we quantify the interdistance between the activated crack nuclei. Images of the type shown in Fig. 17 are analyzed to locate the nucleus of each crack identified as

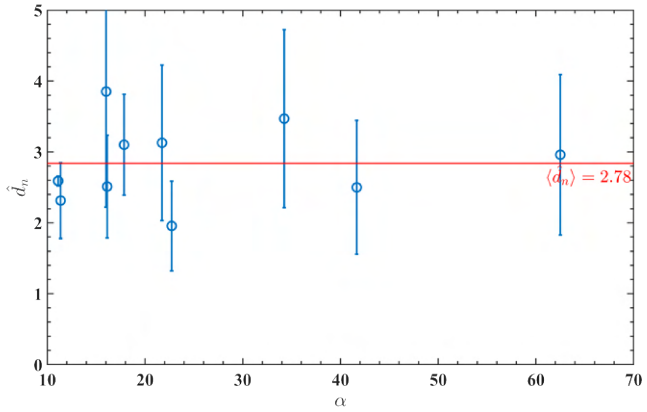

Fig. 22: Spatial distribution of the interdistance of crack nuclei, denoted as $\hat{d}_n$

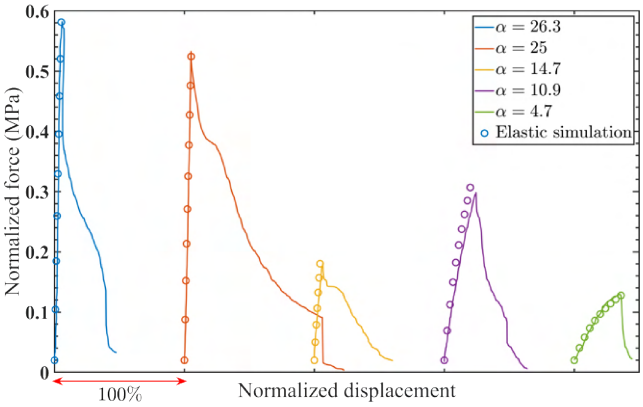

Fig. 23: Collection of the macroscopic stress-strain data for specimens of five different aspect ratios from the experiments (solid lines) and elastic simulation (in circular markers) with the model (1)

the centroid of the crack, and then a Delaunay triangulation is used to determine the distance between the nuclei. This distance d_n is normalized with the specimen thickness to calculate $\hat{d}_n = d_n/T$ (see Fig. 19). The distribution of $\hat{d}_n$ from each experiment (identified with a mean value and a standard deviation), is plotted as a function of the aspect ratio α in Fig. 22. Intriguingly, $\hat{d}_n$ is independent of α to within the scatter at $\langle \hat{d}_n \rangle := mean(\hat{d}_n) = 2.78$. This implies that as a single crack grows to a size comparable to the layer thickness, it depletes the energy in its vicinity and is unable to grow further. A simple analysis of the growth of a single crack in the poker chip specimen has been presented by Hao et al. (2022) indicating this depletion of energy. Nevertheless, a new crack is then nucleated from regions away from the first crack that are still under a triaxial stress state.

6.5 Nucleation threshold stress

Next, we turn our attention to the macroscopic state at nucleation of the first crack. The normalized force vs nominal strain (obtained from the DIC measurements) from five tests representing a range of aspect ratios is shown in Fig. 23. To capture the *nearly* incompressible, hyperelastic material behavior for various grades of cross-linking of the PDMS elastomer, the two-parameter Lopez-Pamies model was used to reproduce the macroscopic load-elongation response of the poker-chip experiment. Here we remark that although the generalized Mooney-Rivlin model is capable of predicting the uniaxial tensile response as indicated in Poulain et al. (2017), it is not able to capture the multiaxial stress states due to the additional stiffening term, (see more details in Gent and Lindley (1959) and Rivlin and Saunders (1951)).

The strain energy density function for the Lopez-Pamies model from Lopez-Pamies (2010) is expressed as

$$W(\mathbf{F}) = \begin{cases} \sum_{i=1}^{i=2} \frac{3^{1-\alpha_i}}{2\alpha_i} \mu_i (I_1^{\alpha_i} - 3^{\alpha_i}) & \text{if } \det \mathbf{F} = 1 \\ +\infty & \text{otherwise} \end{cases} \tag{1}$$

where the principal invariants are defined as $I_1 = \mathrm{Tr}(\mathbf{B})$, with the left Cauchy-Green tensor $\mathbf{B} = \mathbf{F}\mathbf{F}^T$ and deformation gradient $\mathbf{F}$. The corresponding material constants that need be calibrated from the experiment, i.e. μ_i and α_i, are provided in Table. 4.

α_1	α_2	μ_1(MPa)	μ_2(MPa)
-1.02103	1.39107	0.01857	0.03192

Table 4: Coefficients of model (1) for PDMS in 30:1 cross-linking ratio based on the uniaxial tensile experiment Poulain et al. (2017)

The experimental macroscopic stress-strain data from poker-chip tests of different aspect-ratio are compared with the corresponding elastic solutions in Fig. 23.

Clearly the calculated response corresponds closely to the measured response until the onset of the first crack nucleation. This load at nucleation varies significantly with the specimen aspect ratio as shown in Fig. 24. A total of 18 data points are collected to represent the dimensionless normalized force $\hat{S}_{cr}$ ($\hat{S} = S/\mu$) at the onset of nucleation, which can be determined with the protocol as described in Sec. 2. We remark that the data includes specimens with surface crack nucleation if the aspect ratio is small, herein $1/\alpha > 0.2$ (in green

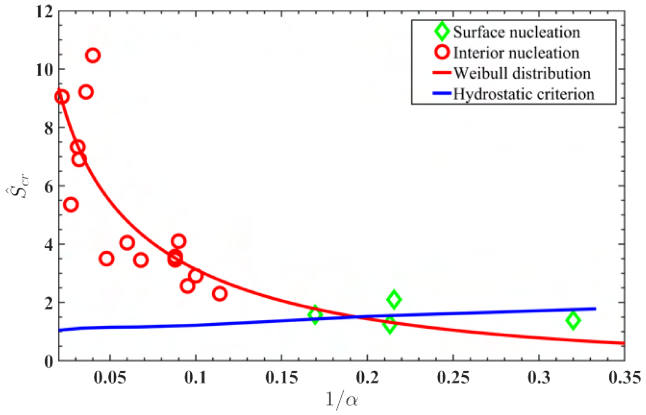

Fig. 24: Critical dimensionless macroscopic stress $\hat{S}_{cr}$ versus aspect ratio, α. Green-diamond markers and red-circle markers denote the samples of surface nucleation and interior nucleation, respectively; the red line represents the fitted threshold with a Weibull function, and the blue line stands for the nucleation threshold based on the hydrostatic criterion.

diamond symbols) as well as specimens with interior nucleation (in red circular symbols).

From Fig. 24, despite some scatter in the range of $1/\alpha < 0.05$, which probably results from the manufacturing variability, it is evident that the critical macroscopic stress $\hat{S}_{cr}$ increases with α; a two-parameter Weibull function is used to get a smooth fitting through the data. The Weibull function and the corresponding parameters are shown in Table. 5. The Weibull function is not intended to imply a defect-driven nucleation criterion, but simply a curve fit to represent the experimental data trend. We remark that the measurements of Gent and Lindley (1959) showed a similar trend for all the materials they considered.

Weibull distribution	$\frac{b}{a}\left(\frac{1}{a\alpha}\right)^{b-1} e^{-(\frac{1}{a\alpha})^b}$
a	7.578
b	0.8348

Table 5: Two-parameter Weibull distribution and fitted parameters

In the classical interpretation of cavitation, following Gent and Lindley (1959), the nucleation threshold stress is identified as that S_{cr} which corresponds to the maximum hydrostatic tension in the specimen reaching the critical point, namely $P_{cr} = 5\mu/2$. Here the model (1) is used for calculating the elastic solution and identifying the critical macroscopic stress. This estimate of the critical stress is shown by the blue line in Fig. 24. While it might appear that for low values of α, the hydrostatic criterion falls along the experimental data (green diamond symbols), crack nucleation in these cases is on the surface and the hydrostatic criterion is not applicable. For larger values of α, nucleation is interior to the specimen, but the prediction of the hydrostatic criterion is far below the experimental values. The hydrostatic criterion does not capture the critical state for the nucleation criterion qualitatively and quantitatively; clearly, the criterion for nucleation of cracks needs to be explored further.

7 Conclusions

A large number of experiments based on the poker-chip geometry, (Gent and Lindley (1959) and Lindsey (1966)) have been performed in the elastomer, polydimethylsiloxane. Typical load-elongation measurements were augmented with optical and x-ray computed tomography imaging at high spatial and adequate temporal resolution. These experiments allowed exploration of the different crack nucleation and growth responses. From this work, we conclude the following:

(i) The nucleation of a crack transitions from surface crack nucleation to interior crack nucleation with increasing aspect ratio (equivalent to increasing constraint); from the experiments, the threshold aspect ratio for this transition is $\alpha_{th} \in (5, 8)$

(ii) The surface cracks always start on the circumferential boundary and close to the rigid boundary; its growth is expected to be dictated by the Griffith criterion, but the nucleation requires an additional criterion based on multiaxial strength, similar to Kumar and Lopez-Pamies (2021)

(iii) The interior nucleation of cracks in three-dimensions has been observed and quantified with an optical microscope and x-ray CT scan. These experiments provide evidence that the first crack does not nucleate where the hydrostatic stress is the largest; instead the critical nucleus is off-center. Moreover, the spatial distribution of the critical crack seems to be independent of the geometric constraint. The mean value of the first nucleus position turns out to be $(R_c, \Phi, Z_c) = (0.225D, \Phi, 0.2T)$, where D and T represent the sample diameter and thickness. The standard deviations of radial and axial coordinates are $0.111D$ and $0.058T$ respectively.

(iv) The different crack growth orientation is also influenced by the thickness: in a thicker specimen the crack tends to propagate in a slanted orientation with respect to the central axis, yet in a thinner specimen the crack tends to grow in a plane that is perpendicular to the central axis.

(v) The fracture event after the burst and growth of the first crack is also dependent on varying confinement:
   (1) if the thickness is large enough, $\alpha < 10$, continuous propagation with a complex geometry is observed; however, the complex geometry can be categorized in three kinds, namely, the slanted, flat and through crack.
   (2) if the thickness is very small, with very large aspect ratio, $\alpha > 40$, the nucleated fracture is not able to continue to grow beyond about a few thicknesses; rather, the subsequent cracks are triggered at a distance from the previous crack(s). This sequential nucleation is uniformly distributed over the entire diameter of the specimen with an inter-distance between the cracks of $\hat{d}_n = 2.78$
   (3) For intermediate aspect ratios, between $10 < \alpha < 40$, there is a competition between the nucleation of a new crack and propagation of the previously nucleated crack.

The experiments described above have revealed what happens during the onset and progression of cracking in the poker-chip specimen. A quantitative criterion for nucleation in PDMS remains to be established; we will address this and simulations of crack growth in a future contribution.

Acknowledgements The financial support of the US National Science Foundation through Grant Number 1900191 is gratefully acknowledged.

Conflict of interest

The authors declare that they have no conflict of interest.

References

Ball JM (1982) Discontinuous equilibrium solutions and cavitation in nonlinear elasticity. Philosophical Transactions of the Royal Society of London Series A, Mathematical and Physical Sciences 306(1496):557–611

Baumberger T, Caroli C, Martina D, Ronsin O (2008) Magic angles and cross-hatching instability in hydrogel fracture. Physical review letters 100(17):178303

Bayraktar E, Bessri K, Bathias C (2008) Deformation behaviour of elastomeric matrix composites under static loading conditions. Engineering Fracture Mechanics 75(9):2695–2706

Buffiere JY, Maire E, Adrien J, Masse JP, Boller E (2010) In situ experiments with X-ray tomography: an attractive tool for experimental mechanics. Experimental Mechanics 50(3):289–305

Busse WF (1938) Physics of rubber as related to the automobile. Journal of Applied Physics 9(7):438–451

Euchler E, Bernhardt R, Schneider K, Heinrich G, Wießner S, Tada T (2020) In situ dilatometry and X-ray microtomography study on the formation and growth of cavities in unfilled styrene-butadiene-rubber vulcanizates subjected to constrained tensile deformation. Polymer 187:122086

Fond C (2001) Cavitation criterion for rubber materials: A review of void-growth models. Journal of Polymer Science, Part B: Polymer Physics 39(17):2081–2096

Gent A (1990) Cavitation in rubber: a cautionary tale. Rubber Chemistry and Technology 63(3):49–53

Gent A, Lindley P (1959) Internal rupture of bonded rubber cylinders in tension. Proceedings of the Royal Society of London Series A Mathematical and Physical Sciences 249(1257):195–205

Gent A, Tompkins D (1969a) Nucleation and growth of gas bubbles in elastomers. Journal of Applied Physics 40(6):2520–2525

Gent A, Tompkins D (1969b) Surface energy effects for small holes or particles in elastomers. Journal of Polymer Science Part A-2: Polymer Physics 7(9):1483–1487

Gent AN, Wang C (1991) Fracture mechanics and cavitation in rubber-like solids. Journal of Materials Science 26(12):3392–3395

Green AE, Zerna W (1992) Theoretical elasticity. Courier Corporation

Hao S, Suo Z, Huang R (2022) Why does an elastomer layer confined between two rigid blocks grow numerous cavities? Submitted

Horgan C, Abeyaratne R (1986) A bifurcation problem for a compressible nonlinearly elastic medium: growth of a micro-void. Journal of Elasticity 16(2):189–200

James RD, Spector SJ (1991) The formation of filamentary voids in solids. Journal of the Mechanics and Physics of Solids 39(6):783–813

Kikinis R, Pieper SD, Vosburgh KG (2014) 3D Slicer: A Platform for Subject-Specific Image Analysis, Visualization, and Clinical Support. Intraoperative Imaging and Image-Guided Therapy pp 277–289

Kumar A, Lopez-Pamies O (2021) The poker-chip experiments of Gent and Lindley (1959) explained. Journal of the Mechanics and Physics of Solids 150:104359

Lakrout H, Sergot P, Creton C (1999) Direct observation of cavitation and fibrillation in a probe tack experiment on model acrylic pressure-sensitive-adhesives. The Journal of Adhesion 69(3-4):307–359

Lefèvre V, Ravi-Chandar K, Lopez-Pamies O (2015) Cavitation in rubber: an elastic instability or a fracture phenomenon? International Journal of Fracture 192(1):1–23

Lin YY, Hui CY (2004) Cavity growth from crack-like defects in soft materials. International Journal of Fracture 126(3):205–221

Lindsey G, Schapery R, Williams M, Zak A (1963) The triaxial tension failure of viscoelastic materials. Tech. rep., CALIFORNIA INST OF TECH PASADENA GRADUATE AERONAUTICAL LABS

Lindsey GH (1966) Hydrostatic tensile fracture of a polyurethane elastomer. Tech. rep., CALIFORNIA INST OF TECH PASADENA GRADUATE AERONAUTICAL LABS

Liu R, Sancaktar E (2018) Identification of crack progression in filled rubber by micro X-ray CT-scan. International Journal of Fatigue 111:144–150

Lopez-Pamies O (2010) A new I_1-based hyperelastic model for rubber elastic materials. Comptes Rendus Mecanique 338(1):3–11

Lopez-Pamies O, Nakamura T, Idiart MI (2011) Cavitation in elastomeric solids: II—Onset-of-cavitation surfaces for Neo-Hookean materials. Journal of the Mechanics and Physics of Solids 59(8):1488–1505

Müller S, Spector SJ (1995) An existence theory for nonlinear elasticity that allows for cavitation. Archive for Rational Mechanics and Analysis 131(1):1–66

Pham K, Ravi-Chandar K (2017) The formation and growth of echelon cracks in brittle materials. International Journal of Fracture 206(2):229–244

Poulain X, Lefèvre V, Lopez-Pamies O, Ravi-Chandar K (2017) Damage in elastomers: nucleation and growth of cavities, micro-cracks, and macro-cracks. International Journal of Fracture 205(1):1–21

Poulain X, Lopez-Pamies O, Ravi-Chandar K (2018) Damage in elastomers: Healing of internally nucleated cavities and micro-cracks. Soft Matter 14(22):4633–4640

Rivlin R, Saunders D (1951) Large elastic deformations of isotropic materials vii. experiments on the deformation of rubber. Philosophical Transactions of the Royal Society of London Series A, Mathematical and Physical Sciences 243(865):251–288

Schindelin J, Arganda-Carreras I, Frise E, Kaynig V, Longair M, Pietzsch T, Preibisch S, Rueden C, Saalfeld S, Schmid B, Tinevez JY, White DJ, Hartenstein V, Eliceiri K, Tomancak P, Cardona A (2012) Fiji: an open-source platform for biological-image analysis. Nature Methods 2012 9:7 9(7):676–682

Shull KR, Creton C (2004) Deformation behavior of thin, compliant layers under tensile loading conditions. Journal of Polymer Science Part B: Polymer Physics 42(22):4023–4043

Sivaloganathan J (1986) Uniqueness of regular and singular equilibria for spherically symmetric problems of nonlinear elasticity. Archive for Rational Mechanics and Analysis 96(2):97–136

Toda H, Maire E, Yamauchi S, Tsuruta H, Hiramatsu T, Kobayashi M (2011) In situ observation of ductile fracture using x-ray tomography technique. Acta Materialia 59(5):1995–2008

Williams ML, Schapery RA (1965) Spherical flaw instability in hydrostatic tension. International Journal of Fracture Mechanics 1(1):64–72

Yerzley FL (1939) Adhesion of neoprene to metal. Industrial & Engineering Chemistry 31(8):950–956